Journal of Nuclear Materials 608 (2025) 155721

Contents lists available at ScienceDirect

Journal of Nuclear Materials

journal homepage: www.elsevier.com/locate/jnucmat

The effect of proton irradiation dose rate on the evolution of microstructure in Zr alloys: A synchrotron microbeam X-ray, TEM, and APT study

Ö. Koç [a,*], R. Thomas [a], B. Jenkins [b,c], C. Hofer [b], Z. Hegedüs [d], U. Lienert [d], R.W. Harrison [a], M. Preuss [a,e], T. Ungár [a], P. Frankel [a]

[a] Department of Materials, The University of Manchester, Oxford Road, M13 9PL, UK
[b] Department of Materials, University of Oxford, Parks Road, Oxford, OX1 3PH, United Kingdom
[c] Université Rouen Normandie, INSA Rouen Normandie, CNRS, Groupe de Physique des Matériaux UMR 6634, F-76000 Rouen, France
[d] Deutsches Elektronen-Synchrotron (DESY), Hamburg, Germany
[e] Department of Materials Science and Engineering, Monash University, Clayton, VIC 3800, Australia

ARTICLE INFO

Keywords:
Zirconium fuel cladding
Transmission electron microscopy (TEM)
Atom probe tomography (APT)
Synchrotron XRD
Proton irradiation

ABSTRACT

Protons are increasingly used as a surrogate for neutrons to study radiation damage of engineering alloys used in the core of a nuclear reactor, enabling high fluences in comparatively short times. However, the accelerated damage rate of protons is usually compensated by an increased irradiation temperature to assist diffusion. To better understand dose rate effects on microstructure evolution during radiation damage, recrystallized Low-Sn ZIRLO and Zircaloy-2 were proton-irradiated to 0.15 dpa at 320 °C using nominal dose rates of 1.3, 2.5, and 5.2 $\times$ 10^{-5} dpa/s. Depth profiling using microbeam synchrotron XRD was conducted across the 30 μm deep irradiated regions for line profile analysis, enabling dislocation line density determination. We found no significant difference in dislocation density among the different dose rates for Zircaloy-2 while Low-Sn ZIRLO displayed dose rate sensitive microstructural evolution. However, Low-Sn ZIRLO exhibited a significantly lower overall dislocation density compared to Zircaloy-2 samples at all dose rates. (S)TEM analysis of the samples showed clear ⟨a⟩ loop alignment in Zircaloy-2, while this was less pronounced in Low-Sn ZIRLO. APT analysis conducted on Low-Sn ZIRLO specimens showed the early onset of irradiation induced nanoclusters of Nb, where the clusters were observed to be comparatively smaller in the sample exposed to high dose rate irradiation. Overall, the integration of different techniques has provided a more comprehensive understanding of the early-stage damage evolution under differing damage accumulation rates.

1. Introduction

The microstructure of materials used in the core of nuclear reactors undergoes significant changes due to constant neutron bombardment at elevated temperature, resulting in irradiation hardening and embrittlement. The most prominent feature of irradiation-induced microstructural evolution is the introduction of vacancy and interstitial point defects through the displacement of atoms due to collision cascades initiated by neutron flux [1,2]. A large proportion of point defects tend to recombine and annihilate at different sinks, depending on sink strengths [1,3]. In zirconium alloys the remaining defects tend to form ⟨a⟩ and ⟨c⟩ type dislocation loops, characterised by their Burgers vectors. While ⟨a⟩ loops are observed at the early stages of irradiation in recrystallized material, ⟨c⟩ loops are only observed at later stages after an incubation dose is reached, typically > 4–5 dpa [3–6]. Importantly, zirconium alloys with typical crystallographic textures exhibit an irradiation-induced volume-conserving shape change, commonly referred to as irradiation induced growth (IIG) [7,8]. An accelerated growth regime is observed at later stages of irradiation and is associated with the onset of ⟨c⟩ loop formation although dislocation loops of ⟨a⟩ type start to form early on [9–11]. Interestingly, it has been observed that the addition of Nb to zirconium alloys results in improved IIG behaviour characterized by a delayed breakaway regime and lower overall growth rates compared to Nb-free alloys such as Zircaloy-2 [7,12]. This growth behaviour in Nb containing alloys has initially been associated with the delayed ⟨c⟩ loop formation [13]. However, Francis et al. [5] showed this was not necessarily the case for proton irradiated Low-Sn ZIRLO. Additionally, Nb-containing alloys, such as Low-Sn

* Corresponding author.
E-mail address: omerfkoc@gmail.com (Ö. Koç).

https://doi.org/10.1016/j.jnucmat.2025.155721
Received 13 September 2024; Received in revised form 27 February 2025; Accepted 27 February 2025
Available online 28 February 2025

ZIRLO, develop irradiation-induced Nb clusters and nano-precipitates that have been postulated to reduce irradiation-induced growth by reducing point defect mobility [14,15]. However, a comprehensive understanding of how Nb nanoclusters influence the development of dislocation structures, and the resulting breakaway growth has remains elusive.

Emulating neutron damage through use of ion irradiation has become a preferred method by many researchers owing to several benefits; such as shorter times necessary to reach comparable dose levels, the easy handling of samples after irradiation and the far lower costs of doing such studies compared to neutron irradiation campaigns [4,16,17]. This is desirable for zirconium research, especially when investigating the irradiation induced growth behaviour and associated ⟨c⟩ loop formation at high doses. Among ion irradiations, protons have a relatively large penetration depth at a given energy ($\geq$ 1 MeV), which produces a reasonably flat damage region over several 10 s of microns when working with zirconium alloys. It has been reported that proton irradiated zirconium alloys exhibit similar microstructural features to those observed in neutron irradiated materials, although this behaviour is strongly influenced by irradiation dose, temperature, and dose rate [4,18]. Specifically, both types of irradiations produce comparable dislocation loop densities, types, and distributions, as well as irradiation-induced chemical redistribution and segregation [4,19]. Additionally, similar levels of irradiation hardening have been observed in both types of materials [20–22]. However, the difference in damage dose rates from different species results in irradiating material for hours/days for protons versus months/years for neutrons, which highlights the need to fully understand the effect of dose rate on microstructural evolution. To account for dose rate difference, an increase in temperature is often applied based on theoretical calculations [4,23]. These calculations for temperature shift assume two types of point defect loss mechanisms are active, namely recombination and sink dominating mechanisms [23]. While this approach is widely used for heavy ion irradiations, its applicability specifically to proton irradiations has not been validated, and there is no clear evidence regarding its accuracy.

To date, studies of ion-based irradiation dose rates have focused mainly on materials other than zirconium suggesting a comparable correlation between neutron-irradiated materials and those irradiated with heavy ions and protons in terms of irradiation induced changes such as hardening and chemical segregation, requiring only a modest temperature increase from in-reactor temperatures [17,24,25]. Overall, irradiation-induced chemical redistribution and dislocation formation appear to follow similar trends between different dose rates [26]. When considering zirconium alloys, Wang et al. [27] reported a similar dislocation density in neutron- and proton-irradiated Zircaloy-4, even though the damage rate differed by two orders of magnitude. Similarly, findings by Saidi et al. [28] on proton-irradiated Zircaloy-4 indicate that there is no significant effect of dose rate on the formation of ⟨a⟩ type dislocation loops irradiated to 0.02 dpa and 1 dpa at 2.89×10^{-6}, 4.34×10^{-6}, and 5.79×10^{-6} dpa/s, though the dose rate range studied here was very narrow.

The characterization of irradiation-induced microstructural evolution is typically performed using transmission electron microscopy (TEM) [2,4,29]. However, the statistical relevance of TEM investigations is limited by sample size and the imaged area. In addition, as loops form from collapsing point defect agglomerations, the loop size distribution will show the highest frequency for the smallest loop size [30]. This renders the quantification of the smallest loops in a transmission image effectively impossible due to the resolution limit [31] creating significant uncertainties for loops below 2–3 nm [32,33]. On the other hand, diffraction line profile analysis has been used to quantify dislocation loop line densities in irradiated materials and is a complementary tool for quantitative dislocation density analysis [34–38]. Diffraction techniques can provide large sampling statistics and can also account for very small features [32]. However, TEM allows observation of loop arrangements and morphology within the visible size range [34,35]. Therefore, the most comprehensive results can be obtained by utilizing both techniques in conjunction.

In this study, we aim to contribute to the understanding of the irradiation response of Low-Sn ZIRLO and Zircaloy-2. Specifically, we carried out proton irradiation experiments on recrystallized Low-Sn ZIRLO and Zircaloy-2 samples at three different dose rates (1.3×10^{-5} (L), 2.5×10^{-5} (M), and 5.2×10^{-5} (H) dpa/s) to investigate the dose rate effect and compare it with previous neutron irradiation studies. We utilized the micro-focused beam synchrotron X-ray diffraction (SXRD) technique to extract information from different damage levels and dose rates by exploiting the proton depth-dependent dose profile. Complementing the SXRD findings, TEM was used to confirm the defect formation in terms of dislocation loops, and Atom Probe Tomography (APT) was used to investigate irradiation-induced changes in the spatial distribution of alloying elements.

2. Experimental methods

2.1. Material and proton irradiation

Recrystallized Low-Sn ZIRLO and Zircaloy-2 with average grain sizes of 6 μm and 15 μm, respectively, were irradiated with protons to a nominal dose of 0.15 dpa (at a depth of approximately 18 μm from the surface) using three different dose rates: 1.3×10^{-5} (L), 2.5×10^{-5} (M), and 5.2×10^{-5} (H) dpa/s. Prior to irradiation, the samples were mechanically polished to achieve a flat, deformation-free surface. The proton irradiation experiments were carried out at The University of Manchester Dalton Cumbrian Facility (DCF) using a 2 MeV beam energy, with the sample temperature maintained at 320 $\pm$ 10 °C, with the other irradiation parameters listed in Table 1 (and given in SI.1). The dose and dose rate calculations were performed using the SRIM (Stopping and Range of Ions in Matter) software package [39], assuming a 40 eV displacement energy for Zr [1]. The nominal 0.15 dpa dose refers to the 60 % damage level of the Bragg peak depth, Fig. 1 together with the hydrogen implantation profile given in blue. Although measurements at the Bragg peak depth may carry greater uncertainty due to hydrogen implantation, the significant temperature gradient between the proton beam-heated surface and the cooler bottom of the sample is expected to drive hydrogen diffusion away from the irradiated region.

Samples for SXRD measurements were cut to a thickness of 0.5 mm using a SiC precision cutting wheel at a slow speed to minimize surface damage. The cross-section of the samples was orientated perpendicular to the irradiated surface to ensure accurate depth-resolved measurements of the damage profile, Fig. 2.

2.2. Synchrotron XRD and line profile analysis (LPA)

SXRD measurements were performed on the P21.2 beamline at the PETRA III synchrotron facility at DESY in Hamburg, Germany [40], with a beam energy of 67.5 keV. The experiment was carried out in transmission geometry, with a beam focussed to a height of 2 μm for adequate resolution in the irradiation direction, and a width of 200 μm to maximise the number of grains illuminated at each depth. Depth scans were

Table 1
Proton irradiation parameters for Zircaloy-2 and Low Sn ZIRLO samples.

Dose rate (dpa/s)	Designation	Nominal dose (dpa)	Irradiated area (mm^2)	Current (μA)	Irradiation duration (hrs)
1.3×10^{-5}	Low dose rate (L)	0.15	10×12	22.3	3.3
2.5×10^{-5}	Medium dose rate (M)	0.15	3.5×8.5	11	1.7
5.2×10^{-5}	High dose rate (H)	0.15	3.5×5	13.5	0.79

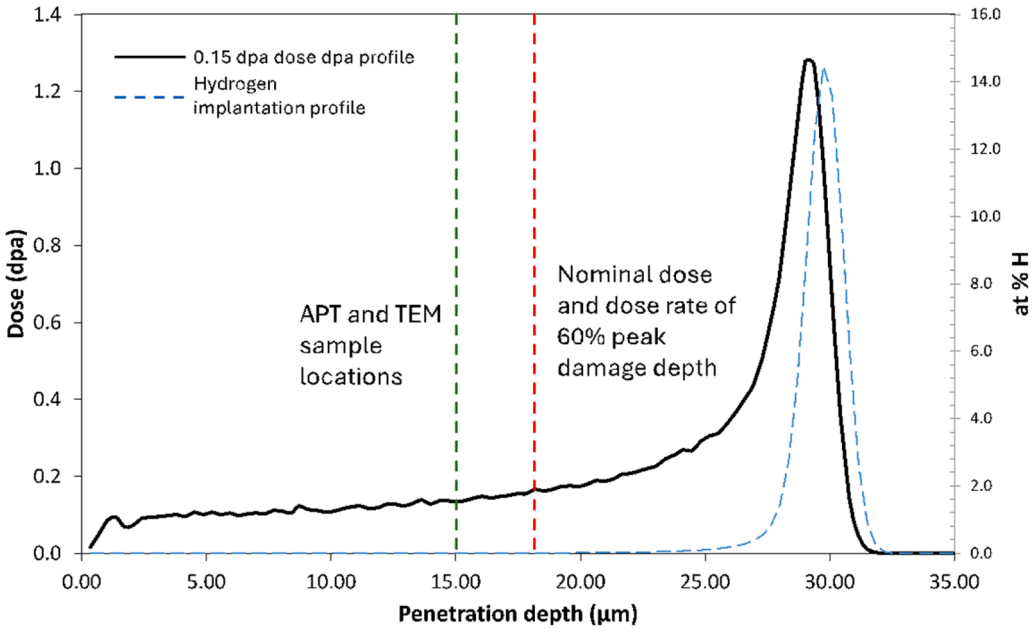

Fig. 1. SRIM software package generated dose profile assuming 40 eV displacement damage for Zr with 2 MeV protons. The red line shows the 60 % Bragg peak depth where the nominal dpa values were reported from, while the green dashed line indicates the APT and TEM sample extraction depths.

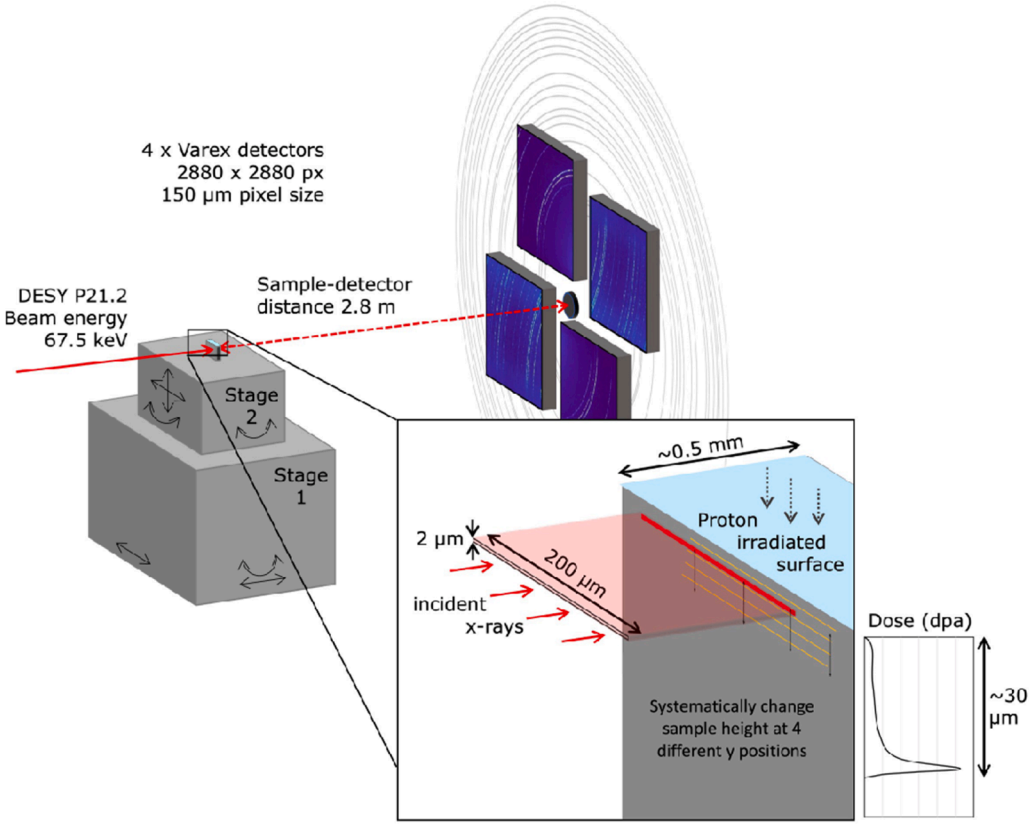

Fig. 2. Schematic representation of the X-ray diffraction depth profiling experiment set-up used at the DESY P21.2 beamline.

performed by translating the sample upwards in steps of 2 μm (to match the beam height) up to a maximum depth probed of 60 μm below the sample surface. This measurement was repeated for four different horizontal positions. Diffraction images were captured by four Varex XRD 4343CT detectors placed around the direct beam, at 2.8 m downstream of the sample. An illustration of the experiment setup is given in Fig. 2. Calibration of detector positions and distance were performed using a CeO_2 calibrant and the integration of images into line profiles were performed using the freely available PyFAI python library [41].

In undeformed, recrystallized materials, the diffraction patterns exhibit narrow, symmetrical reflections however irradiation-induced dislocation loops cause peaks to broaden [42–44]. The broadening of

the zirconium diffraction peaks was evaluated using the freely available Convolutional Multiple Whole Profile (CMWP) software (version 210, 616) to calculate the line density of irradiation-induced dislocation loops [45]. The background function for the SXRD profiles were generated using a spline, the points for which were calculated using an algorithm based on datapoints between the reflections (SI.3).

The CMWP method convolutes all the broadening effects using the calculated peak patterns and compares them to the measured diffraction line profile via fitting of established physical functions [46–48] to extract numerical data on microstructural features, such as dislocation density. Further details about the diffraction line profile analysis and CMWP fitting method can be found in [32,45,49]. Here, only the portion related to the strain broadening due to dislocation loops is summarised.

The Krivoglaz-Wilkens model [46] calculates the Fourier transform of the strain broadened profile as follows:

$$FT\left(I_{hkl}^{D}\right)(L) = \exp\left[-\rho\left(\frac{\pi b}{2}\right)^{2} g^{2}\overline{C}L^{2}f(\eta)\right] \quad (1)$$

where ρ is the dislocation density, b is the magnitude of the Burgers vector, g is the absolute value of diffraction vector, $\overline{C}$ is the *hkl* dependent average contrast factor of dislocations, L is the Fourier variable and $f(\eta)$ is the strain function derived by Wilkens [46], where $\eta = L/R_e$ and R_e is the effective outer cut-off radius of dislocations. For characterizing dislocation arrangements or dipole characters, Wilkens introduced the dimension free arrangement parameter M, given as $M = R_e\sqrt{\rho}$. When comparing systems with the same dislocation densities the different arrangements can be well characterized by the M parameter which carries the dipole character information of dislocation structures. More organised dislocation arrangement and strong dipole character result in a diffraction peak with a long tail and gives M values around 1 or smaller in the analysis. In contrast, a weak dipole character and loosely distributed dislocations results in a short diffraction tail providing M values much larger than 1 in the analysis [32,50,51]. The individual errors are calculated for each parameter during the fitting procedure by CMWP using the via p% (confidence interval parameter) fractions of the weighted sum of the square of the residuals (WSSR) produced by the Monte-Carlo algorithm. The estimated error values from the line profile analysis were determined using the confidence interval with a significance level of $P = 3.5$. This confidence interval provides a measure of the uncertainty associated with the line profile analysis results.

The averaged contrast factor $\overline{C}_{hk.l}$ is given by the following equation relating to the hexagonal materials [52]:

$$\overline{C}_{hk.l} = \overline{C}_{hk.0}\left(1 + q_1 x + q_2 x^2\right), \quad (2)$$

where $x=(2/3)(l/ga)^2$, $\overline{C}_{hk.0}$ is the average contrast factor for the *hk.0* (prismatic) reflections, $q_1$and q_2 are depending on slip mode and Burgers vectors. Furthermore, q_1, q_2, and $\overline{C}_{hk.0}$ are dependent on the elastic constant of the materials as well as the dislocation types present [52]. Theoretical contrast factors for irradiation-induced ⟨a⟩ and ⟨c⟩ type dislocation loops are given in [18,50].

2.3. Electron microscopy

TEM foils were extracted from the samples and thinned using an FEI Helios plasma focused ion beam (p)FIB microscope with the samples held at −130 °C using a cryo-stage to minimise hydride formation and FIB damage [53]. TEM foils were lifted out from the cross-section of the samples to characterize the same regions as those measured using XRD. The bulk of the thinning process was conducted at a 30 kV accelerating voltage and beam currents of 0.23 nA and 74 pA. Final thinning and cleaning were performed at 2 kV with 19 pA until transparency was achieved under 5 kV electron beam imaging. Electron microscopy investigations were carried out using a Thermo Fisher Scientific Talos F200X field-emission TEM at 200 kV. Bright-field (S)TEM images of ⟨a⟩ loops were captured on the $<11\bar{2}0>$ zone axis and loop alignment was confirmed with 1–2 grains from each condition.

2.4. Atom probe tomography (APT)

Initial lift out and welding steps were carried out at ambient temperatures using an FEI Helios plasma (p)FIB microscope while further thinning of the tips were performed at cryo temperatures (−130 °C) with the same microscope. To prevent large dpa variations throughout the analysis volumes and to maintain microstructural consistency, lift outs for APT tips were performed from 15 to 20 μm depth of the samples at which SRIM predicted dpa is calculated to be ~0.2 dpa. APT tip sharpening started using a circular milling pattern with 5 μm outer and 1.2 μm inner diameter with 0.23 nA 30 kV using Xe^+. This was followed by smaller circular pattern milling of 2 μm outer and 0.35 μm inner diameter with 74 pA 30 kV Xe^+. After achieving around 100 nm tip diameter, final cleaning with 19 pA 2 kV Xe^+ were performed. More details are given in [54,55].

APT analyses were conducted on a Cameca LEAP-5000 XR instrument at the University of Oxford. Analyses were performed at 60 K using laser-pulsing mode, with a laser energy of 20 or 40 pJ and a pulse frequency of either 125 or 200 kHz. Detection rates of between 0.003 and 0.005 ions per pulse were used. APT reconstructions and data analyses were performed using IVAS 3.8.16, whilst peak overlaps were solved and compositional analyses were performed using AtomProbeLab v0.2.4 [56]. Nb-rich nanoclusters were identified and extracted from the experimental data using isosurfaces [57], with threshold values selected to ensure that individual Nb-rich features were identified and not merged together. A threshold value of 2.0 at % Nb was applied to each of the experimental datasets such that direct comparisons could be made. Number densities, volume fractions, and cluster radii were calculated using the equations in Ref. [58] modified for HCP-Zr instead of BCC-Fe. In total, 2–3 tips were analysed from each condition.

3. Results

3.1. XRD line profile analysis

For examination of the diffraction line profiles, the first 20 α-Zr diffraction peaks were utilized. Fig. 3 presents a qualitative comparison of the prismatic $11\bar{2}0$ peaks from three different depths of the samples corresponding to different dpa levels for Low-Sn ZIRLO and Zircaloy-2. In addition, the prismatic $11\bar{2}0$ peaks are shown for three different dose rates with the dose rate corresponding to a depth of approximately 18 μm from the surface.

Fig. 3 shows a progressive broadening in the $11\bar{2}0$ peak profiles of both alloys with dpa. It is noticeable that the broadening of the peak tails is far more pronounced than broadening at full width half maximum (FWHM). In contrast to Zircaloy-2, the Low-Sn ZIRLO exhibits less peak broadening. A closer inspection of Fig. 3 also shows that both alloys display greater broadening of the tails towards the lower 2θ side, i.e., larger d-spacing, resulting in slightly asymmetric peak shape, which may imply a dominance of one loop nature over the other as vacancy or interstitial. Zirconium alloys neutron and proton irradiated to higher dpa levels than studied here have previously shown to display satellite peaks within the tail regions [34,59], which cannot be seen here.

Fig. 4 plots the dislocation line density profiles based on CMWP calculations as a function of depth for Low-Sn ZIRLO and Zircaloy-2 for the low, medium and high dose rates. The shaded blue region represents the SRIM calculated damage profile. Fig. 4a highlights that dislocation density at pre-Bragg peak depths, i.e., in the plateau, is only marginally higher than in the non-irradiated state. In contrast, Zircaloy-2 (Fig. 4b) exhibits an increase of dislocation line density up to 30 μm, followed by a drop to non-irradiated levels that coincides with the overall predicted depth of the proton penetration. These two alloys exhibit different

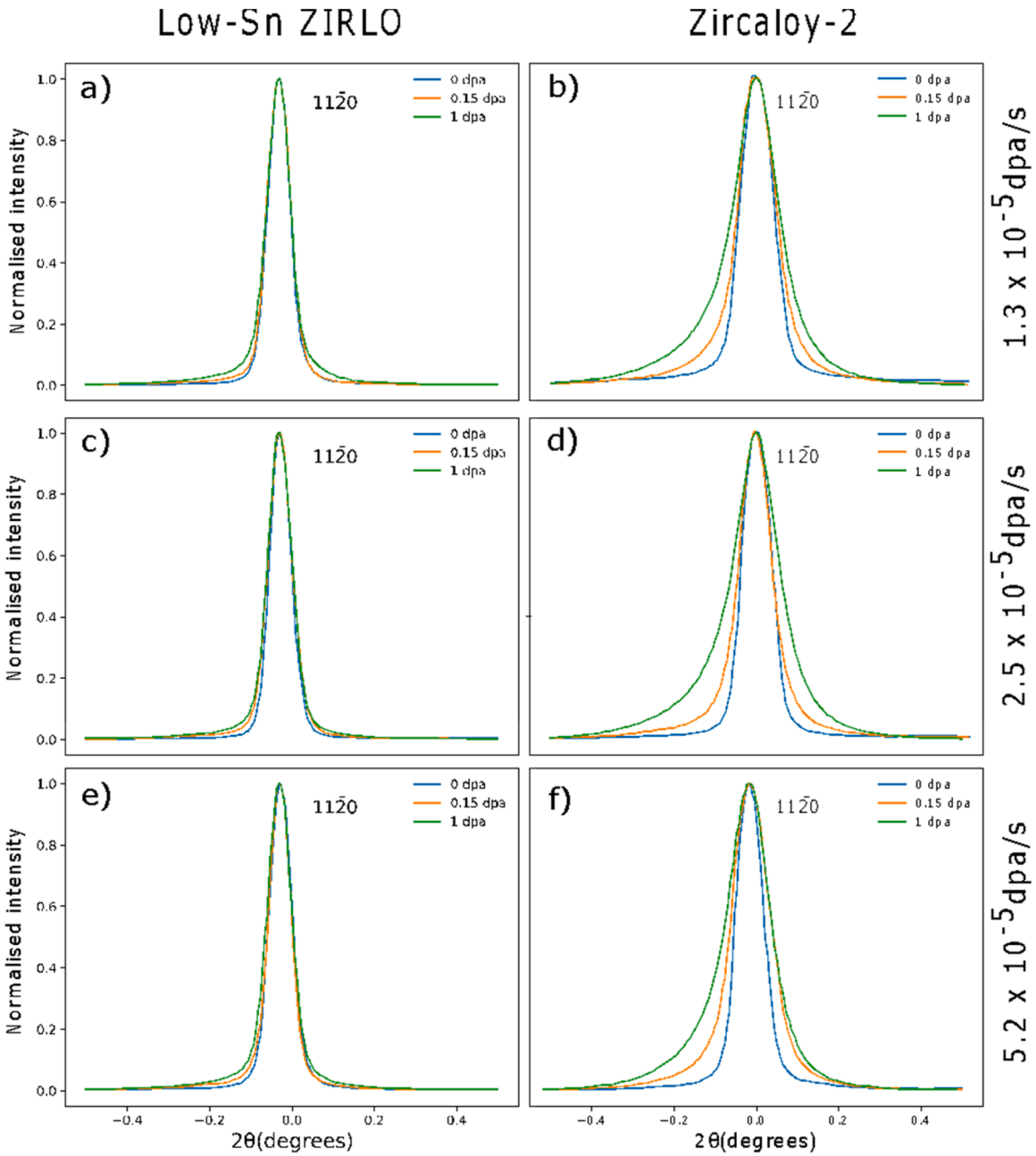

Fig. 3. <$11\bar{2}0$> XRD peaks show the damage dependent broadening as a function of dose and dose rate (proton penetration depth) for a), c), and e) Low-Sn ZIRLO (L), (M), and (H) respectively, b), d), and f) Zircaloy-2 (L), (M), and (H) respectively. The peak centres have been aligned with the 0 dpa peak (which is from the non-irradiated state that was collected beyond 35 μm depth of the samples) for easy comparison of peak shape and breadth change.

dislocation densities at the Bragg peak after exposure to the low and medium dose rates, with Low-Sn ZIRLO samples displaying lower dislocation line densities than Zircaloy-2. For the Low-Sn ZIRLO exposed to the highest dose rate, the dislocation line density at the Bragg peak is comparable to that of Zircaloy-2.

Fig. 5a and b illustrate the M parameter as a function of depth for both alloys at all three dose rates. Notably, when the dislocation line density is very low, the M arrangement parameter is large, surpassing the upper limit of the y-axis on the graphs (in the range between 15 and 250). When the M value is on the order of 10 and larger this indicates very weak dipole character of dislocation loops, ie. few randomly distributed dislocations without having dipole character and can be treated equally [60]. This large M value indicates very high uncertainty and is no longer a useful parameter. Therefore, the upper limit is introduced for better presentation of the overall data especially around Bragg peak depth where the strong dipole character is observed characterised by very small M values. This is particularly apparent in the non-irradiated areas of all samples and in the plateau region of Low-Sn ZIRLO. Fig. 5c and d show M values excluding data points for dislocation density lower than 0.3×10^{14} m^{-2} which is the dislocation density value representing the non-irradiated state that was collected beyond 35 μm depth of the samples. This shows that for Low-Sn ZIRLO, except for the high dose rate sample within the vicinity of the Bragg peak region, the dislocation loops are not only of low line density but also have an extremely weak dipole character.

Fig. 6 illustrates the dislocation density evolution of the two alloys with respect to dose. It is important to remind the reader at this stage that while the data are separated into low, medium and high dose rate, the dose rates vary substantially within a sample when going from low to high dpa, as shown in Fig. 7. In case of Low-Sn ZIRLO, an early increase

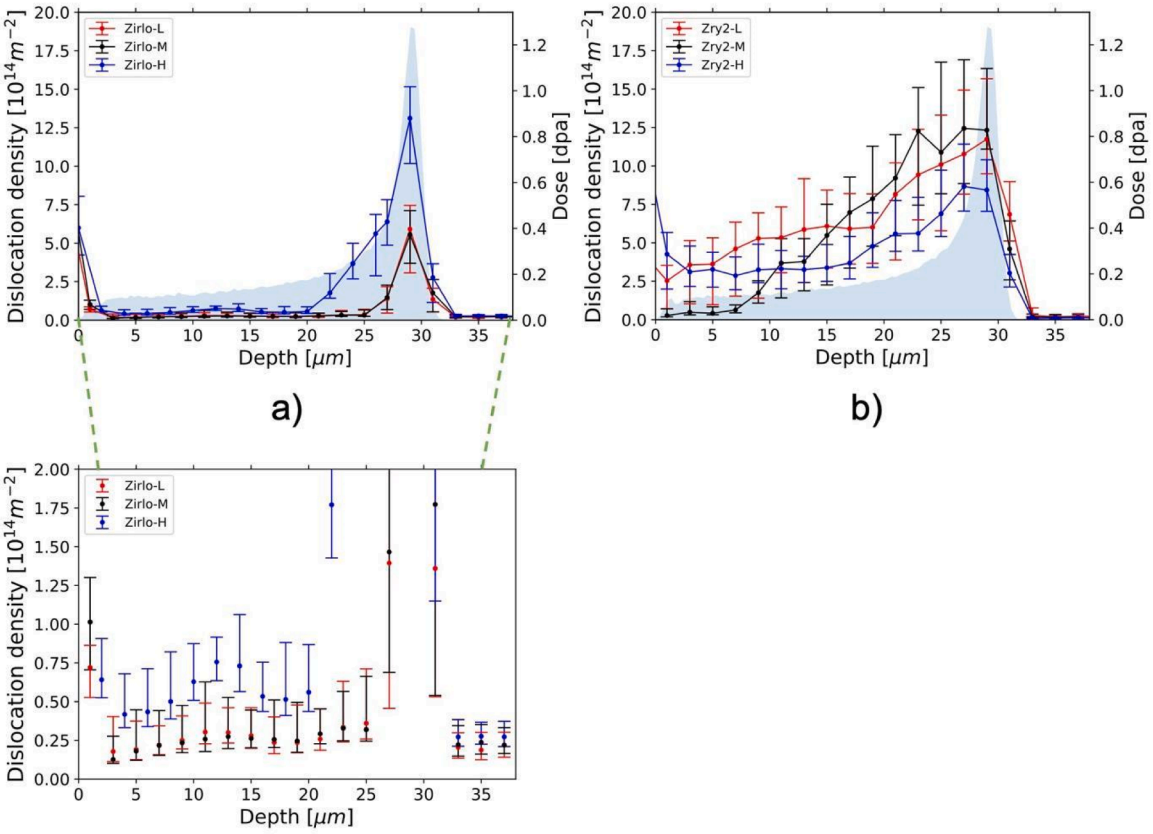

Fig. 4. Dislocation density versus distance from the irradiated sample surface at different dose rates for a) Low-Sn ZIRLO (including magnified version for better visualisation of the plateau region), and b) Zircaloy-2. Blue shaded areas show SRIM calculated dose profiles with the corresponding dpa on the right Y axis.

in dislocation line density is observed for the high dose rate. For the low and medium dose rate Low-Sn ZIRLO samples, almost no change of line density is seen up to about 0.4 dpa after which the values start to rise. In contrast, Zircaloy-2 shows a very steep increase in dislocation line density for all dose rates from the lowest dpa level and tends to plateau between 0.3 and 0.4 dpa. Additionally, no significant difference can be observed in the samples for the three different dose rates in Zircaloy-2. Fig. 8 illustrates the dislocation densities from Low-Sn ZIRLO samples with the corresponding dose rate from each location indicating a clear dose rate dependence specifically at higher doses.

3.2. STEM dislocation loop imaging

STEM images of Zircaloy-2 (L) are presented in Fig. 9, which were extracted at about 15 μm from the surface, as indicated in Fig. 1. Fig. 9a was obtained by using $\mathbf{g} = 0002$ diffraction condition demonstrating that the sample does not contain dislocation loops with a c-component according to the $\mathbf{g}.\boldsymbol{b} = 0$ invisibility criterion (see SI.4 for Low-Sn ZIRLO). Fig. 9b is an image down the $<11\bar{2}0>$ zone axis, which shows $\langle a \rangle$ loops with a $\frac{1}{3}\langle 11\bar{2}0 \rangle$ type Burgers vector [4,5]. Fig. 10 and Fig. 11 display STEM images captured from Low-Sn ZIRLO and Zircaloy-2 samples, respectively, for each dose rate condition. Although there is a strong alignment of $\langle a \rangle$ loops in all three instances of Zircaloy-2 samples, the $\langle a \rangle$ loop alignment is not pronounced in Low-Sn ZIRLO, which agrees with findings in [5] for higher dose. The level of alignment was quantified to some extent by measuring the separation distances between the rows of $\langle a \rangle$ loops which is 88 nm, 83 nm, and 75 nm for Zircaloy-2 (L), Zircaloy-2 (M), and Zircaloy-2 (H) respectively. However, spacing of the rows of $<a>$-loops is not periodic, and the rows themselves are discontinuous making the quantification challenging and less representative, especially in Low-Sn ZIRLO. Hence the same quantification could not be performed for Low-Sn ZIRLO.

3.3. Nb nanoclustering findings by APT

The APT examination of Zircaloy-2 samples did not reveal any significant clustering of Fe or Sn, nor did it indicate the presence of anti-correlative banding (which was previously observed on the length scales of 15–20 nm [19]) in the vicinity of aligned $\langle a \rangle$ loops, Fig. 12. This finding contrasts with the typically reported observations in irradiated Zircaloy-2 samples at higher doses after proton and neutron irradiations [4,19]. An analysis of these findings, as demonstrated in Fig. 12, pertains specifically to the sample subjected to high-dose-rate irradiation.

The APT measurements for Low-Sn ZIRLO samples, carried out at a similar distance from the surface as the TEM foils, confirmed the presence of irradiation-induced nanoclustering of Nb, Fig. 13. The cluster measurement statistics are provided in Table 2. The results confirm the irradiation induced chemical evolution in the samples, even at this early damage level (0.15–0.2 dpa). Nanoscale clustering of Nb was observed for all three different dose rates, along with some enrichment of Sn and Fe in these clusters (see Table 2) compared to the matrix composition. Notably, despite the comparable number density of these clusters, the mean cluster radius in the high dose rate irradiated sample was observed to be smaller in contrast to the low and medium dose rate irradiated samples. Fig. 14 displays histogram plots of the cluster sizes after different dose rate irradiations. In addition, the Nb content within the clusters decreases slightly with increasing dose rate. The Nb content in the Low-Sn ZIRLO matrix was determined to be approximately 0.45 at.% from non-irradiated tip measurements, which falls within the range (0.29–0.49 wt.%) reported for the solubility of Nb in binary Zr-Nb alloys [61,62] while this number averages to slightly <0.1 at.% when nanoclusters were excluded in the irradiated condition. Table 3 presents the matrix composition of the Low-Sn ZIRLO alloys at different dose rates

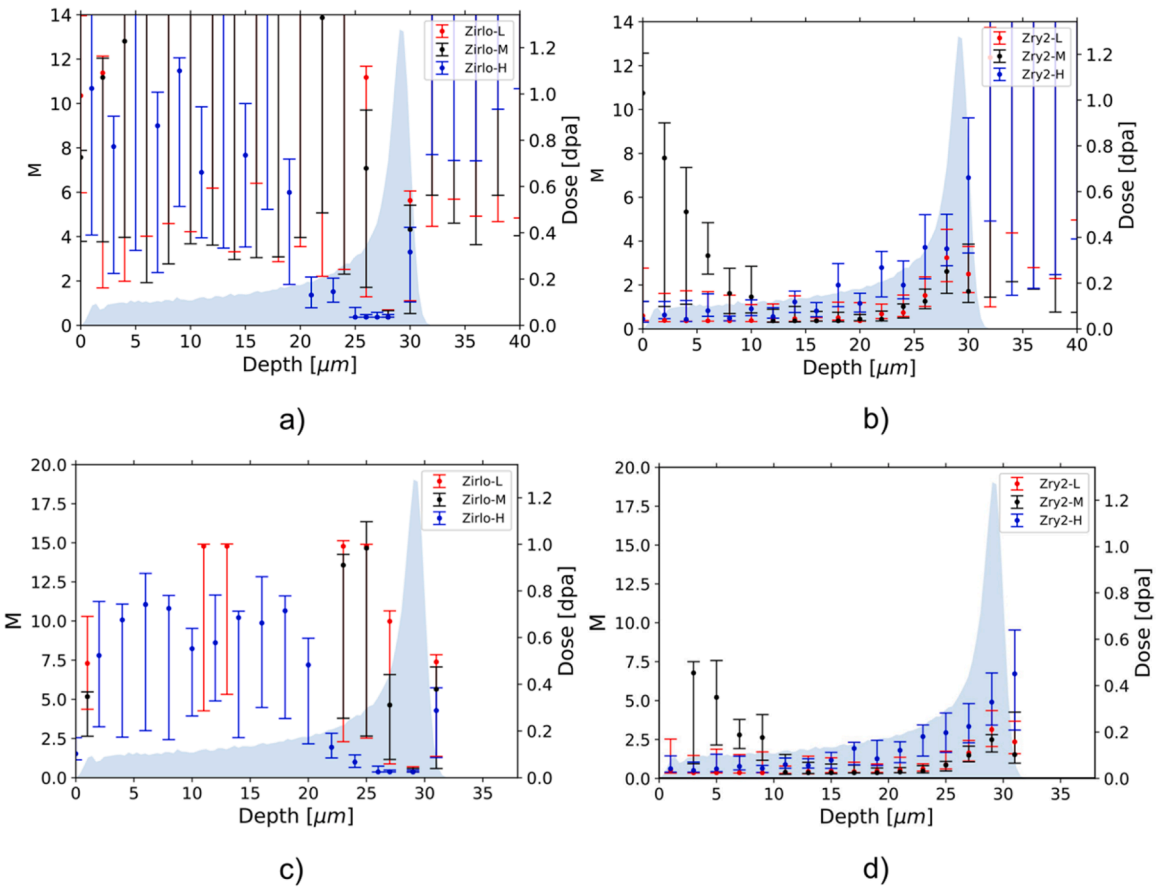

Fig. 5. Arrangement parameter M versus proton irradiation depth at different dose rates for a) Low-Sn ZIRLO, b) Zircaloy-2 and in c) Low-Sn ZIRLO and d) Zircaloy-2 data points excluded for dislocation density values below 0.3 × 10 ^{14} m^{-2}. The error bars represent a measure of the uncertainty associated with the line profile analysis results relating to the dipole character of dislocation loops.

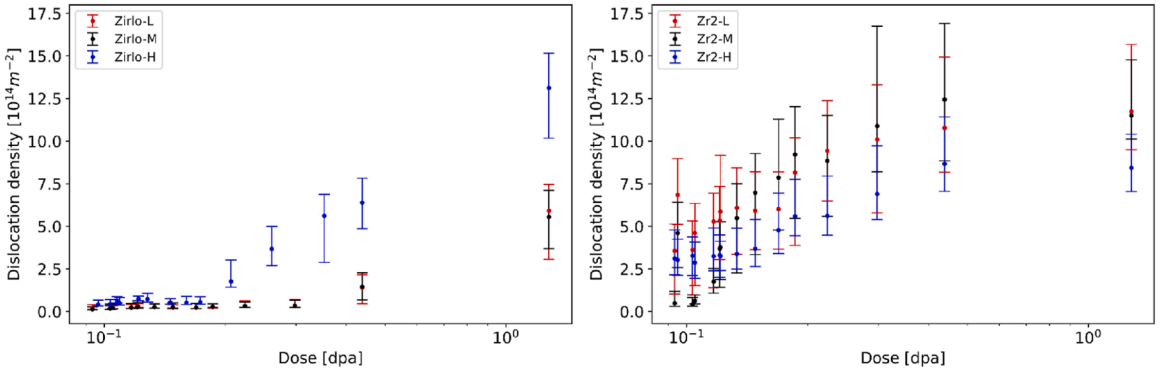

Fig. 6. Dislocation density versus dose plots of a) Low-Sn ZIRLO, and b) Zircaloy-2 for different dose rates.

excluding nanoclusters.

4. Discussion

4.1. Dislocation density difference between Low-Sn ZIRLO and Zircaloy-2

A significant difference in dislocation density was observed between Low-Sn ZIRLO and Zircaloy-2 at all three nominal dose rates within the plateau region before the Bragg peak, corresponding to dpa levels below 0.4 dpa. This observed difference provides insight into the distinct irradiation response and microstructural evolution of Zircaloy-2 and Low-Sn ZIRLO during the very early stage of irradiation. Specifically, even at pre-breakaway doses, Low-Sn ZIRLO exhibits lower irradiation-induced growth compared to Zircaloy-2, as reported by Yagnik et al. [12], in a neutron irradiation campaign. Additionally, at higher doses, Low-Sn ZIRLO appears to have inhibited ⟨c⟩ loop formation, as documented in previous studies [12,63,64]. These investigations focused on dpa levels above 2 dpa of proton and neutron irradiations [5,65]. In our study, although the dislocation density of Low-Sn ZIRLO is significantly lower than that of Zircaloy-2 below around 0.2 dpa, it increases rapidly at the Bragg peak depth corresponding to ~1 dpa, as shown in Fig. 6, which demonstrates an increasing dislocation density trend as a function of dpa and dose rate. The difference in the early stages of damage might be related to the early formation of irradiation induced Nb nanoclusters

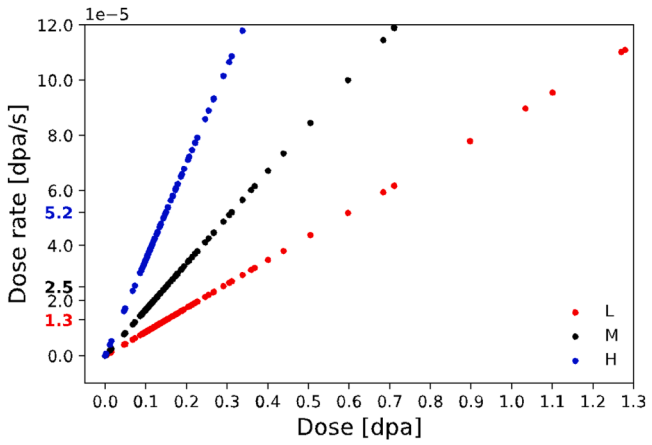

Fig. 7. Dose rate vs dpa plot for 2 MeV proton irradiated zirconium with three different nominal dose rates, irradiated to the same nominal dpa as predicted by SRIM calculations.

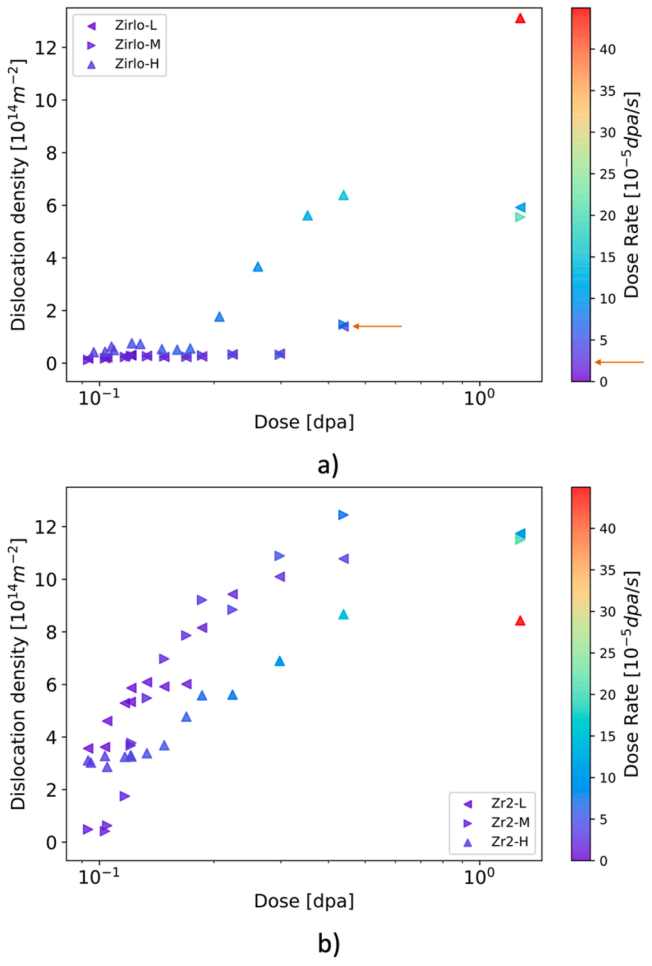

Fig. 8. Plot of dislocation density versus dose for proton-irradiated a) Low-Sn ZIRLO, and b) Zircaloy-2 samples, where marker colour indicates the dose rate. Arrows indicate the lowest dose rate (2.5×10^{-5} dpa/s) at which the dislocation density formation is observed in Low-Sn ZIRLO samples.

observed in Low-Sn ZIRLO samples, which is thought to be the main factor in the improved IIG and corrosion properties of these alloys at higher dpa [5,66].

The dislocation density difference between Low-Sn ZIRLO and Zircaloy-2 can be primarily attributed to the presence of Nb and the former alloy's smaller grain size, both of which are influenced by Nb content. This is consistent with the findings of Yang et al. [22], who reported variations in dislocation density in Nb-containing alloys with differing Nb content and attributed these effects to the formation of Nb precipitates and the reduced grain sizes associated with Nb addition.

There is a difference in the grain sizes of Low-Sn ZIRLO and Zircaloy-2 which are 6 μm and 15 μm respectively. Nb plays a multifaceted role in the microstructural evolution of Low-Sn ZIRLO. First, it contributes to grain refinement, which in turn enhances the sink strength by increasing the grain boundary area. This elevated sink strength enhances point defect annihilation, especially at grain boundaries, promoting the formation of smaller dislocation loops. Second, during irradiation, Nb forms nanoclusters from the initial stages as shown in the present study, which serve as sinks for point defects and allow the nucleation of smaller loops while inhibiting their growth. Consequently, point defects in Low-Sn ZIRLO are more frequently intercepted both by grain boundaries and by Nb nanoclusters, leading to more efficient defect annihilation and stabilization of smaller dislocation loop structures [14]. However, Nb nanoclusters form at very low doses (0.15dpa) with the irradiation which is thought to be the dominant effect compared to grain size.

Furthermore, the investigated dose rate regime spans from 0.79×10^{-5} dpa/s to 44.9×10^{-5} dpa/s covering a broad range which was enabled by the micro beam SXRD depth profiling across the damage profile. This large dose rate range allowed the observation of the relationship between dose rate, dose, and dislocation density after irradiation. The large variation in dose rates at different irradiation depths resulted in differing dpa levels for similar dose rates, as shown in Fig. 8. Within the investigated dose rate range, no significant difference in dislocation density was observed for Zircaloy-2 while there was a distinct difference for Low-Sn ZIRLO when comparing the medium and highest dose rate, Fig. 6 and Fig. 8. When considering Fig. 6, it is important to keep in mind that with increasing dpa level, the dose rate also increases as highlighted in Fig. 7. Additionally, Fig. 8 employs a colour heat map to depict dose rate variation with proton penetration depth in correlation with dislocation density versus dpa plots. The visualizations offer a clear representation of the relationship between proton dose rates and dislocation density at different penetration depths for Low-Sn Zirlo while Zircaloy-2 doesn't show such a clear dose rate dependent behaviour. Hence, for Low-Sn ZIRLO, there seems to be a threshold dose rate of about 2.5×10^{-5} dpa/s (annotated in the Fig. 8a) below which slower dose rates do not produce any observable dislocation line density regardless of the dpa level. Going beyond such a dose rate, the dislocation line density increases with dose. It does so most dramatically for the high dose rate sample where the dose rate increase is also most dramatic as shown in Fig. 7. Hence it seems that the potential point sink effect of Nb clusters stops working when a critical dose rate is exceeded, which might be related to altered Nb clustering kinetics due to ballistic mixing. In the phase-field modelling study by Kharchenko et al. [67], neutron irradiation induced Nb nanoprecipitation in the 2 % Nb-Zr system was investigated. The model predicted that at elevated dose rates, the number density of precipitates increased after an initial incubation period (~0.8 dpa). However, the precipitates formed under these conditions were smaller compared to those formed at lower dose rates, consistent with the observations in the present study which is thought to be the main factor in the different dislocation density observation. This behaviour suggests that while high dose rates enhance nucleation, they concurrently suppress growth due to enhanced ballistic mixing. Notably, the dose rate range investigated in Kharchenko et al. [67].'s study was two orders of magnitude smaller than the proton irradiation dose rate range explored in the current work. This significant difference may contribute to the discrepancies observed, particularly regarding the presence of an incubation period prior to Nb cluster formation.

Another notable finding from their simulations was the existence of a dose rate threshold for precipitate stability. Below this threshold, precipitation progressed with irradiation, leading to an increase in average

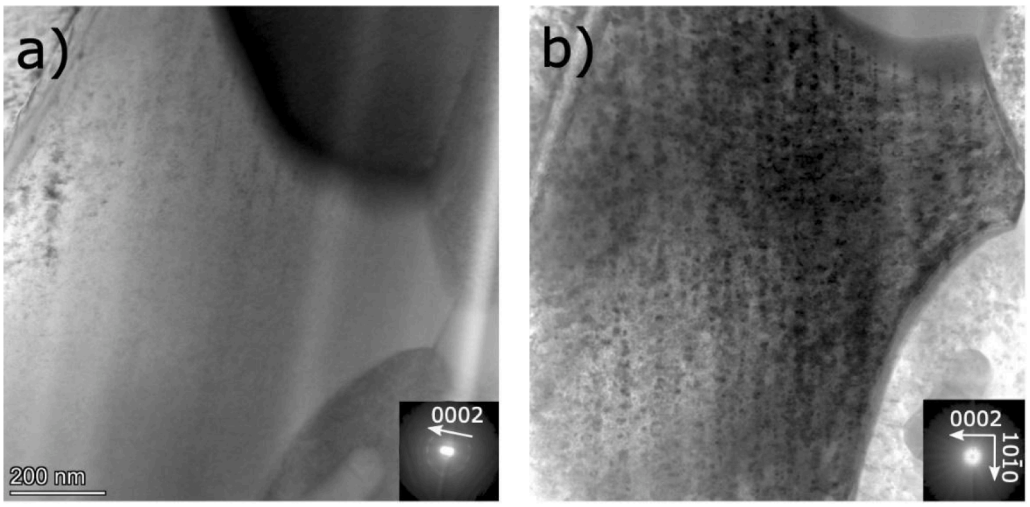

Fig. 9. BF-STEM images obtained from 0.15 dpa proton irradiated Zircaloy-2 (L) sample where a) and b) shows the same region with crystal aligned with the g = 0002 systematic row of reflections and down the <11$\bar{2}$0> zone axis respectively.

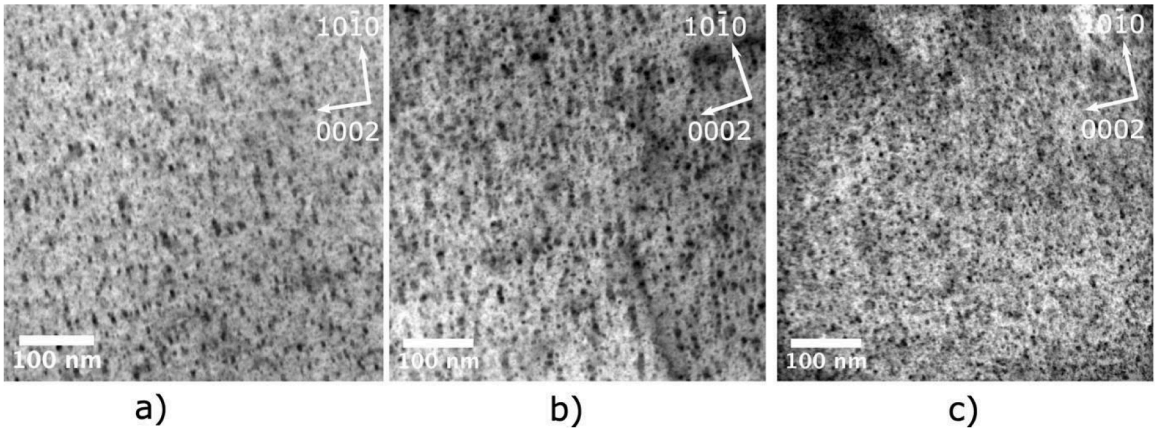

Fig. 10. BF-STEM images from 3 different dose rate 0.15 dpa proton irradiated Low-Sn ZIRLO taken down the <11$\bar{2}$0> zone axis, a) ZIRLO-L, b) ZIRLO-M, and c) ZIRLO-H.

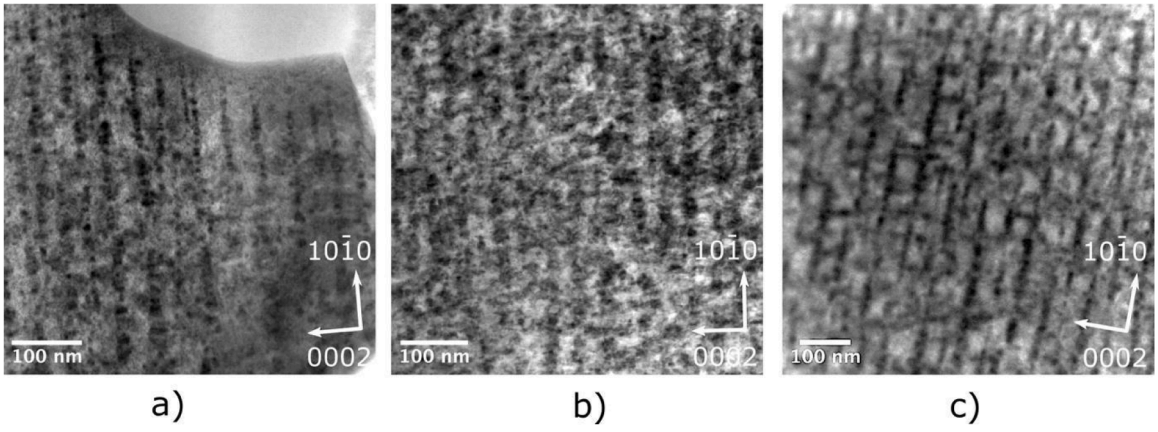

Fig. 11. BF-STEM images from 3 different dose rate 0.15 dpa proton irradiated Zircaloy-2 taken down the <11$\bar{2}$0> zone axis, a) Zry2-L, b) Zry2-M, and c) Zry2-H.

precipitate size. However, exceeding the threshold caused precipitate dissolution, driven by the dominant effect of ballistic mixing. This behaviour aligns well with the findings of the present study. Moreover, there are other systems, such as Fe-Cr alloys, where the increasing dose rate was found to delay the precipitation of α′ particles, both experimentally and through computational modelling [68,69]. These studies demonstrated that an increase in dose rate leads to the disappearance of Cr-rich α′ phases that typically form during irradiation, analogous to the observation of smaller Nb nanoclusters in the current study. In particular, high dose rate irradiation resulted in smaller Nb

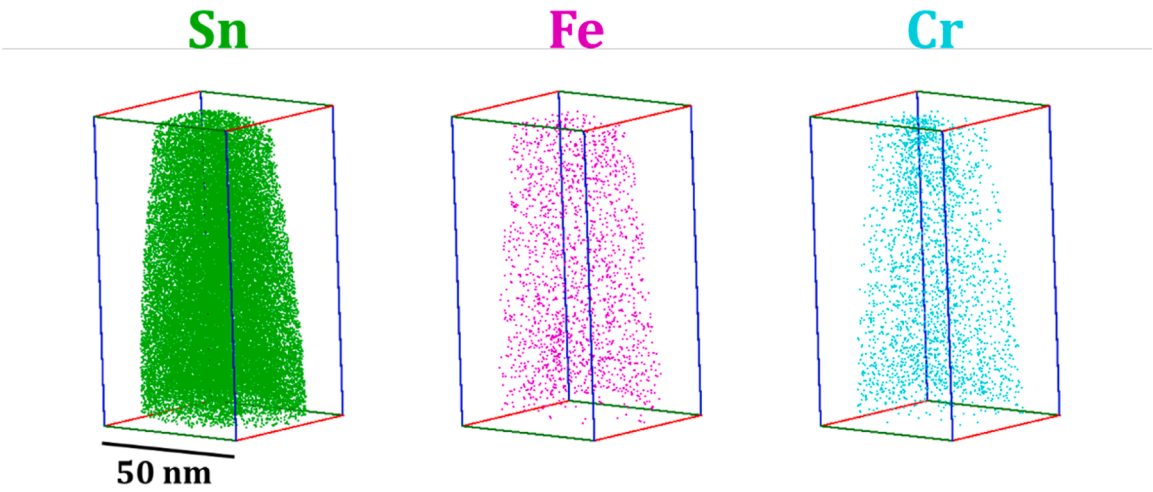

Fig. 12. APT data from high dose rate (5.2×10^{-5} dpa/s) 0.2 dpa proton irradiated Zircaloy-2 with homogeneous distribution of alloying elements. Zr is not displayed for better visibility.

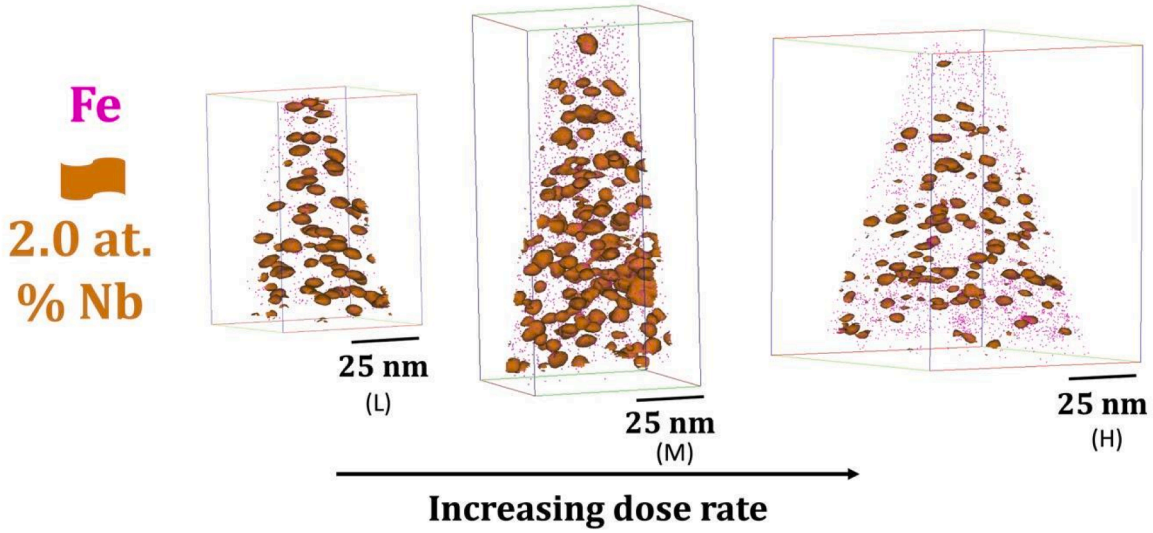

Fig. 13. APT data from low, medium, and high dose rate irradiated Low-Sn ZIRLO samples displaying Nb nanoclusters with the 2.0 at % Nb isosurfaces and Fe atoms without any nanoclustering.

Table 2
APT irradiation-induced cluster analysis for Low-Sn ZIRLO specimens subjected to three different dose rates. The analyses were conducted on tips (2–3 tips were analysed from each condition) extracted from the plateau regions of the samples corresponding to around 0.2 dpa, with the reported compositions specifically originating from nano clusters. N.B. The uncertainty in the size measurements is the standard error of the measured cluster sizes for each condition.

Name	Dose rate (dpa/s)	Size (nm)	Number density (m^{-3})	Elements (at. %)			
				Zr	Nb	Fe	Sn
L	1.3×10^{-5} dpa/s	2.37 ± 0.11	$4.4 \pm 0.7 \times 10^{23}$	92.75 ± 0.29	6.06 ± 0.12	0.24 ± 0.03	0.96 ± 0.08
M	2.5×10^{-5} dpa/s	2.75 ± 0.11	3.8 ± 0.8 x 10^{23}	92.61 ± 0.32	5.56 ± 0.11	0.08 ± 0.06	1.05 ± 0.06
H	5.2×10^{-5} dpa/s	1.69 ± 0.05	4.8 ± 0.5 x 10^{23}	92.47 ± 0.2	4.92 ± 0.07	0.01 ± 0.02	0.84 ± 0.04

nanoclusters similar to the observations in Fe-Cr system which may be linked to higher dose rates limiting the time for diffusion. Additionally, other mechanisms including ballistic mixing may be contributing as well. Neutron irradiations in these alloys which have very low dose rates were found to result in larger and more Cr-rich clusters compared to ion irradiations at higher dose rates [68]. This suggests that ballistic mixing plays a lesser role at lower dose rate irradiations such as neutron irradiation. Similarly, Harrison et al. [70] irradiated Fe14Cr alloy with He, Ne, and Kr ions with different energies and found that α′ precipitation was hindered when the primary effect is increased ballistic mixing at higher energy and dose rates. Based on these findings, the interplay between the production rate of point defects, their recombination, ballistic mixing, and dissolution emerges as a critical relationship in affecting Nb nanocluster formation during irradiation. At sufficiently high dose rates, with less time for nucleation and growth, Nb dissolution is expected to dominate the process, potentially preventing the formation of Nb nanoclusters up to a certain damage level (dpa) which would enhance dislocation loop formation. Additionally, Table 1 shows that the Nb-content within the clusters decreases for the samples with increasing dose rate. It might also be the case that with increasing dose rate the production rate of point defects simply exceeds the absorption

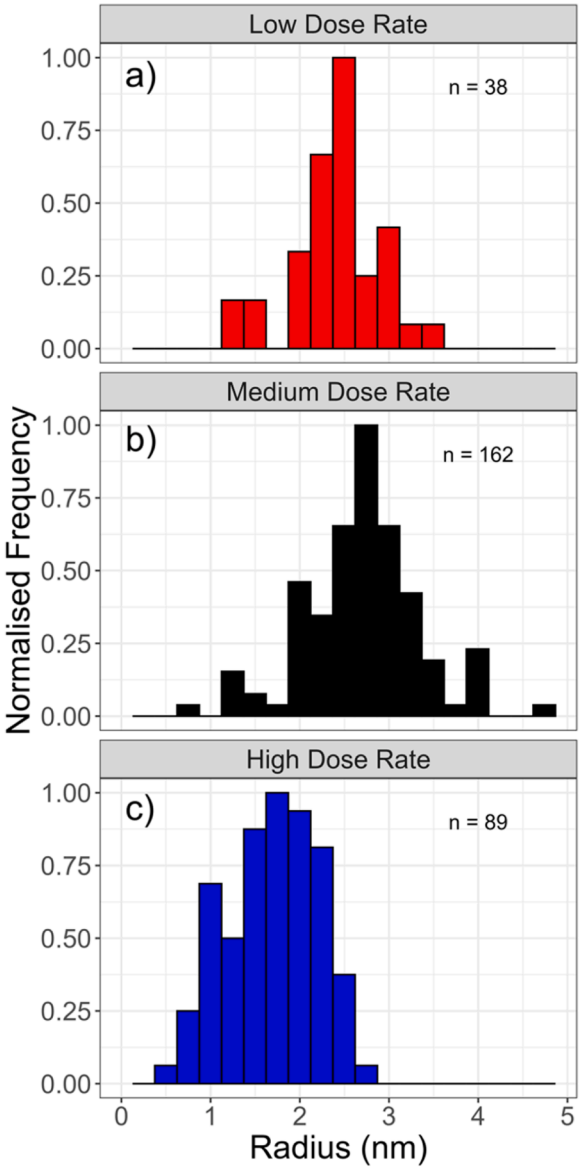

Fig. 14. Histogram plots of irradiation induced nanocluster sizes from low (a), medium (b), and high (c) dose rate irradiated Low-Sn ZIRLO specimens.

Table 3
APT matrix composition results for the Low-Sn ZIRLO specimens from three different dose rates excluding nanoclusters. Additionally, baseline, non-irradiated sample APT data is given as comparison which doesn't contain Nb nanoclusters.

Name	Dose rate (dpa/s)	Elements (at. %)		
		Nb	Fe	Sn
L	1.3×10^{-5} dpa/s	0.052 ± 0.008	0.029 ± 0.005	0.549 ± 0.011
M	2.5×10^{-5} dpa/s	0.085 ± 0.012	0.027 ± 0.004	0.639 ± 0.012
H	5.2×10^{-5} dpa/s	0.078 ± 0.008	0.056 ± 0.005	0.511 ± 0.007
Baseline	–	0.45 ± 0.07	0 ± 0.01	0.51 ± 0.02

rate of the Nb clusters regardless of their composition. Furthermore, this phenomenon can be elucidated by the observed decrease in Nb nanocluster size in Low-Sn ZIRLO (H) sample. For each dose rate, the Nb nanocluster number density in irradiated Low-Sn ZIRLO samples is very similar. However, nanocluster size is noticeably smaller in the high dose rate irradiated sample. Consequently, the smaller nanoclusters, despite similar quantities, create fewer defect sink regions within a given area. This likely promotes dislocation loop formation in the nanocluster-free matrix regions of the high dose rate irradiated sample.

Fig. 15 presents a comparative analysis of nanocluster size and number density derived from the current study and the literature, combining both ion and neutron irradiations. Our hypothesis suggests that the overall reduction trend in nanocluster number density with increasing dose in all samples presented in Fig. 15, coupled with the increase in their size, can be attributed to the coalescence of Nb nanoclusters. This coalescence leads to larger clusters, subsequently diminishing their overall number density and resulting in increased distances between clusters. The greater distance between defect sinks facilitates the formation and growth of dislocation loops, like the effect of higher dose rates as discussed earlier. This effect is particularly pronounced in our study, where the observed trends align with those illustrated in Fig. 15. Specifically, Figs. 6 and 13, along with Table 2, demonstrate that the high-dose-rate irradiated samples exhibit smaller nanocluster sizes and greater spacing between nanoclusters. This structural configuration corresponds to an increased dislocation density, as highlighted in Fig. 6 (and is presented in SI.5).

The predominantly smaller nanocluster sizes observed in ion-irradiated materials, as compared to their neutron-irradiated counterparts, are primarily attributed to differences in dose rates (data in Fig. 15 suggests that neutron irradiation promotes larger cluster sizes compared to ion irradiation, which results in smaller clusters). This hypothesis aligns with findings from Yu et al. [71], who observed a similar influence of dose rate in their neutron irradiation study on a ZrNb alloy. Beyond this, fundamental distinctions exist between the irradiating species. For instance, ions, being charged particles, interact with target atoms through distinct mechanisms [72]. One critical difference is the resulting damage morphology, particularly in terms of cascades and isolated Frenkel pairs [1]. In proton irradiation, smaller and more widely separated cascades are produced, contrasting with the damage evolution during neutron irradiation [1]. Nevertheless, protons effectively generate point defects and have been shown to replicate the microstructural features observed in neutron-irradiated Zr alloys [4,5,27]. However, limitations arise when considering phenomena that are highly dependent on dose rate.

4.2. *Early-stage irradiation induced alignment of ⟨a⟩ loops*

The alignment of ⟨a⟩ loops in zirconium alloys after irradiation is a well-documented phenomenon in the literature [4,29,76]. The rafting of dislocation loops has also been observed in other metals such as Cu, Ni, and Fe after ion and neutron irradiations [77–79]. Harte et al. [4] proposed that the alignment of loops is a gradual process with increasing dpa after proton irradiation. However, the present study shows that ⟨a⟩ loop alignment can be observed as early as 0.15 dpa in Zircaloy-2, for all three dose rates, but to a far lesser extent in Low-Sn ZIRLO. Interestingly, Sn segregation has been observed in higher dose samples to anticorrelate with loop alignment and it has been unclear if this segregation in fact drives the alignment [4,19]. In the present study, the relatively short irradiation times did not lead to Sn segregation suggesting that the anticorrelation observed in previous work is not a driver but an eventual consequence of ⟨a⟩ loop alignment. It was previously argued that observations of loop and void alignment in irradiated nickel is related to the minimization of strain energy [79]. Molecular dynamic simulation studies on zirconium by Dai et al. [80] found that the total energy of loops is higher when they are aligned. It has been suggested previously that the observed differences in loop alignment between Zircaloy-2 and Low-Sn ZIRLO can be attributed to the effects of Nb nanoclustering in Low-Sn ZIRLO samples [5,81].

The present study reveals that Nb nanoclusters begin to form at an early stage, potentially suppressing ⟨a⟩ loop alignment by encouraging defect recombination and delaying their alignment process [15]. The mechanism behind the less pronounced ⟨a⟩ loop alignment and reduced dislocation loop formation can be attributed to the restricted mobility of

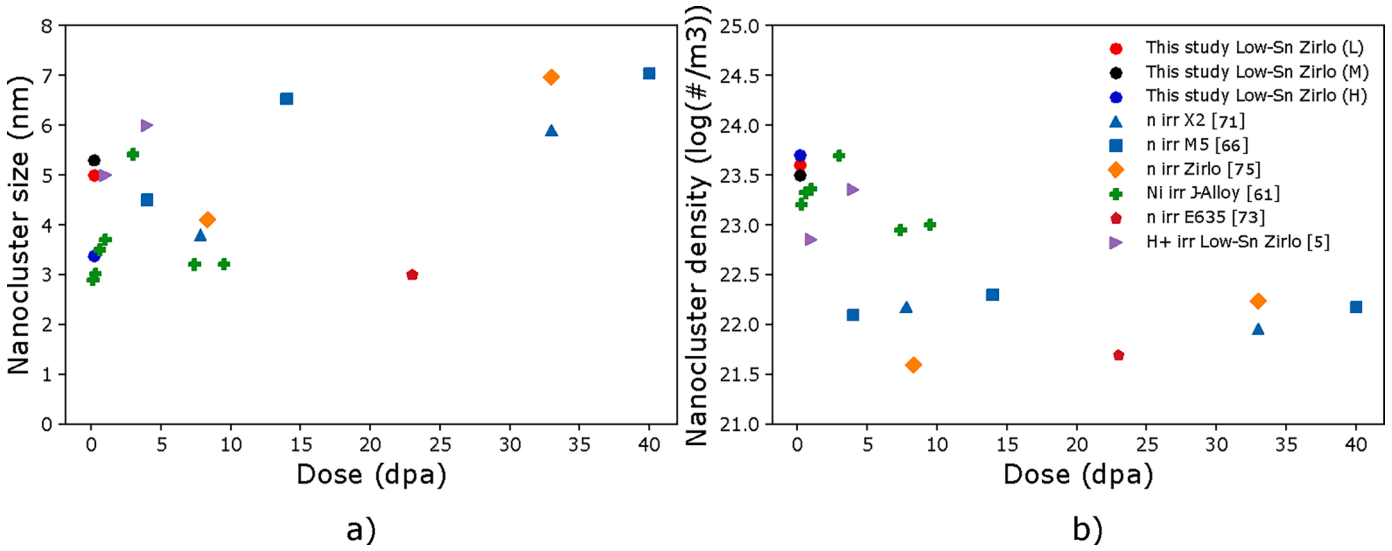

Fig. 15. Irradiation induced nanocluster size (diameter) (a), and nanocluster number density (b) from irradiated Nb containing Zr alloys [66,71,73–75] with the dose rates ranging from 1.1 × 10^{-6} dpa/s to 6.5 × 10^{-4} dpa/s and irradiation temperatures between 300 – 350 °C.

⟨a⟩ loops caused by Nb nanoclusters. These clusters, present in high concentrations, act as significant barriers, effectively immobilizing the ⟨a⟩ loops and preventing them from achieving their most energetically favourable configuration, alignment [5]. Similarly, the work by Gurovich et al. [82] reports limited ⟨a⟩ loop alignment in Zr-1 % Nb alloy subjected to 1.5 dpa neutron irradiation, with the alignment intensity increasing with higher irradiation doses. Their findings also indicate the formation of Nb nanoclusters, which become more prominent at doses of 5.6 and 9.1 dpa, where nanocluster alignment intensifies. Additionally, the dislocation density in their study is observed to saturate at approximately 1.5 dpa, closely aligning with the peak damage levels (~1.2–1.3 dpa) observed in the present study.

For non-Nb-containing alloys, such as Zircaloy-2 and Zircaloy-4, ⟨a⟩ loop density saturation has been reported to occur at doses of 0.15–1 dpa [36,83], while for pure zirconium, theoretical calculations suggest saturation occurs between 5 and 10 dpa [84]. In a related study, Shishov et al. [85] investigated the effects of Fe and Sn in Nb-containing alloys and demonstrated a higher degree of ⟨a⟩ loop alignment after neutron irradiation compared to Nb-only alloys, alongside a delay in Nb nanocluster formation. With the significant differences between Zircaloy-2 and Low-Sn ZIRLO at early damage levels, it would be valuable to examine their dose rate-dependent behaviours at higher dpa levels (>4–5 dpa), where <c>-loop formation typically occurs and is associated with the onset of breakaway growth during irradiation [7]. Low-Sn ZIRLO demonstrates superior performance under irradiation, associated with its Nb content and the formation of nanoclusters, which may interact with ⟨c⟩ loops in a dose rate-dependent manner [5]. Additionally, studying a broader range of dose rates spanning several orders of magnitude would be valuable.

5. Conclusions

Zircaloy-2 and Low-Sn ZIRLO were proton irradiated to a nominal dose of 0.15 dpa with three different nominal dose rates of 1.3, 2.5, and 5.2 × 10^{-5} dpa/s at 320 °C.

- At the early stages of proton irradiation, a significant lower dislocation density was found for Low-Sn ZIRLO irradiated at low and medium dose rate compared to Zircaloy-2 irradiated at any dose rate. It is suggested that the very early Nb nanocluster formation in Low-Sn ZIRLO creates very effective point defect sinks at the early stage of irradiation.
- At high dose rates, Low-Sn ZIRLO shows a much faster rise in dislocation density as a function of dose and dose rate than at low and medium dose rates though it is still slower compared to Zircaloy-2. It is suggested that at the highest dose rate the formation of Nb nanoclusters becomes less apparent due to several factors such as limited diffusion time.
- Low-Sn ZIRLO was found to be much more irradiation dose rate sensitive under the investigated conditions (dose rate, irradiation temperature, and the proton irradiation) compared to Zircaloy-2 in terms of dislocation density and nanocluster formation.
- Strong ⟨a⟩ loop alignment was observed in Zircaloy-2 at an early stage of 0.15 dpa with no evidence of chemical segregation and Sn banding suggesting that chemical segregation is not the cause for ⟨a⟩ loop alignment.
- <*a*> loop alignment was found to be far less pronounced in Low-Sn ZIRLO which may be attributed to the early formation of small Nb nanoclusters.
- Similar Nb nanocluster formation was observed in Low-Sn ZIRLO at all three dose rates though the cluster size decreases and the Nb content within the clusters decreases with increasing dose rate.

In summary, proton irradiation emerges as a valuable methodology for emulating the consequences of neutron irradiation on chemical segregation, specifically with regard to the formation of Nb nanoclusters in Low-Sn ZIRLO and their influence on dislocation formation. This technique serves as a suitable surrogate for investigating material behaviour in conditions similar to neutron irradiation, thereby providing crucial insights into the underlying mechanisms governing chemical segregation and dislocation dynamics in Zr alloys. Nevertheless, in consideration of the outcomes presented in this study, careful planning of proton irradiation experiments is imperative. This is particularly crucial to ensure an accurate representation of neutron-induced damage in Low-Sn ZIRLO, specifically with respect to dislocation loop formation and Nb nanocluster development given the significantly faster dose rates, compared to neutron irradiations, achieved through this technique.

CRediT authorship contribution statement

Ö. Koç: Writing – original draft, Methodology, Investigation, Formal analysis, Data curation, Conceptualization. **R. Thomas:** Writing – review & editing, Software, Methodology, Investigation, Formal analysis,

Data curation, Conceptualization. **B. Jenkins:** Writing – review & editing, Visualization, Software, Methodology, Investigation, Data curation. **C. Hofer:** Writing – review & editing, Software, Methodology, Investigation. **Z. Hegedüs:** Writing – review & editing, Investigation, Formal analysis. **U. Lienert:** Writing – review & editing, Software, Investigation, Formal analysis. **R.W. Harrison:** Writing – review & editing, Supervision, Methodology, Formal analysis, Conceptualization. **M. Preuss:** Writing – review & editing, Supervision, Project administration, Methodology, Investigation, Funding acquisition, Formal analysis, Conceptualization. **T. Ungár:** Writing – review & editing, Validation, Methodology, Investigation, Formal analysis, Conceptualization. **P. Frankel:** Writing – review & editing, Supervision, Project administration, Methodology, Investigation, Funding acquisition, Formal analysis, Conceptualization.

Declaration of competing interest

The authors declare that they have no known competing financial interests or personal relationships that could have appeared to influence the work reported in this paper.

Acknowledgements

The authors would like to thank the Engineering and Physical Sciences Research Council UK for funding the study through the MIDAS (Mechanistic understanding of Irradiation Damage in fuel Assemblies) programme grant (EP/S01702X/1). Ömer Koç was supported by a grant from the Republic of Türkiye, Ministry of National Education. We acknowledge the support of the Dalton Cumbrian Facility (DCF), the experimental base of The University of Manchester's Dalton Nuclear Institute and a partner in the National Nuclear User Facility, the EPSRC UK National Ion Beam Centre and the Henry Royce Institute. We acknowledge DESY (Hamburg, Germany), a member of the Helmholtz Association HGF, for the provision of experimental facilities. Parts of this research were carried out at the PETRA III beamline P21.2. The atom probe facilities at the University of Oxford are funded by the Engineering and Physical Sciences Research Council (EPSRC) grants EP/M022803/1 and EP/T011505/1. We acknowledge Westinghouse for providing the zirconium alloy samples. The microscopy was carried out at the University of Manchester EM Centre and the authors would like to thank the technical support staff. This work was supported by the Henry Royce Institute for Advanced Materials, funded through EPSRC grants EP/R00661X/1, EP/S019367/1, EP/P025021/1 and EP/P025498/1. figures

Supplementary materials

Supplementary material associated with this article can be found, in the online version, at doi:10.1016/j.jnucmat.2025.155721.

Data availability

Data will be made available on request.

References

[1] G.S. Was, Fundamentals of radiation materials science: metals and alloys, second edition, 2016. https://doi.org/10.1007/978-1-4939-3438-6.
[2] F. Onimus, S. Doriot, J.L. Béchade, Radiation effects in zirconium alloys, 2020. https://doi.org/10.1016/B978-0-12-803581-8.11759-X.
[3] R.B. Adamson, Effects of neutron irradiation on microstructure and properties of Zircaloy, ASTM Spec. Tech. Publ. (2000) 15–31, https://doi.org/10.1520/stp14292s.
[4] A. Harte, D. Jädernäs, M. Topping, P. Frankel, C.P. Race, J. Romero, L. Hallstadius, E.C. Darby, M. Preuss, The effect of matrix chemistry on dislocation evolution in an irradiated Zr alloy, Acta Mater (2017), https://doi.org/10.1016/j.actamat.2017.03.024.
[5] E. Francis, R.P. Babu, A. Harte, T.L. Martin, P. Frankel, D. Jädernäs, J. Romero, L. Hallstadius, P.A.J. Bagot, M.P. Moody, M. Preuss, Effect of Nb and Fe on damage evolution in a Zr-alloy during proton and neutron irradiation, Acta Mater (2019), https://doi.org/10.1016/j.actamat.2018.12.021.
[6] B. Christiaen, C. Domain, L. Thuinet, A. Ambard, A. Legris, A new scenario for ⟨c⟩ vacancy loop formation in zirconium based on atomic-scale modeling, Acta Mater 179 (2019) 93–106, https://doi.org/10.1016/j.actamat.2019.07.030.
[7] R.B. Adamson, C.E. Coleman, M. Griffiths, Irradiation creep and growth of zirconium alloys: a critical review, J. Nucl. Mater. 521 (2019) 167–244, https://doi.org/10.1016/j.jnucmat.2019.04.021.
[8] R. Adamson, Irradiation growth of Zircaloy, Zircon. Nucl. Ind. (1977), https://doi.org/10.1520/stp35579s, 326-326–18.
[9] G.J.C. Carpenter, R.H. Zee, A. Rogerson, Irradiation growth of zirconium single crystals: a review, J. Nucl. Mater. (1988), https://doi.org/10.1016/0022-3115(88)90087-6.
[10] Y. Idrees, E.M. Francis, Z. Yao, A. Korinek, M.A. Kirk, M. Sattari, M. Preuss, M. R. Daymond, Effects of alloying elements on the formation of <c>-component loops in Zr alloy Excel under heavy ion irradiation, J. Mater. Res. 30 (2015) 1310–1334, https://doi.org/10.1557/jmr.2015.89.
[11] R.A. Holt, R.W. Gilbert, ⟨c⟩ component dislocations in annealed Zircaloy irradiated at about 570 K, J. Nucl. Mater. 137 (1986) 185–189, https://doi.org/10.1016/0022-3115(86)90218-7.
[12] S. Yagnik, R. Adamson, G. Kobylyansky, J.-H. Chen, D. Gilbon, S. Ishimoto, T. Fukuda, L. Hallstadius, A. Obukhov, S. Mahmood, Effect of alloying elements, cold work, and hydrogen on the irradiation-induced growth behavior of zirconium alloy variants, Zircon. Nucl. Ind. 18th Int. Symp. (2018) 748–795, https://doi.org/10.1520/stp159720160040.
[13] V. Shishov, M. Peregud, A. Nikulina, P. Shebaldov, A. Tselischev, A. Novoselov, G. Kobylyansky, Z. Ostrovsky, V. Shamardin, Influence of zirconium alloy chemical composition on microstructure formation and irradiation induced growth, Zircon. Nucl. Ind. Thirteen. Int. Symp. (2002), https://doi.org/10.1520/stp11415s, 758-758–22.
[14] H.L. Yang, Y. Matsukawa, S. Kano, Z.G. Duan, K. Murakami, H. Abe, Investigation on microstructural evolution and hardening mechanism in dilute Zr[sbnd]Nb binary alloys, J. Nucl. Mater. 481 (2016) 117–124, https://doi.org/10.1016/j.jnucmat.2016.09.016.
[15] M. Christensen, W. Wolf, C.M. Freeman, E. Wimmer, R.B. Adamson, L. Hallstadius, P.E. Cantonwine, E.V. Mader, Effect of alloying elements on the properties of Zr and the Zr-H system, J. Nucl. Mater. (2014), https://doi.org/10.1016/j.jnucmat.2013.10.040.
[16] M. Topping, A. Harte, T. Ungár, C.P. Race, S. Dumbill, P. Frankel, M. Preuss, The effect of irradiation temperature on damage structures in proton-irradiated zirconium alloys, J. Nucl. Mater. 514 (2019) 358–367, https://doi.org/10.1016/j.jnucmat.2018.12.006.
[17] C.D. Hardie, C.A. Williams, S. Xu, S.G. Roberts, Effects of irradiation temperature and dose rate on the mechanical properties of self-ion implanted Fe and Fe-Cr alloys, J. Nucl. Mater. 439 (2013) 33–40, https://doi.org/10.1016/j.jnucmat.2013.03.052.
[18] T. Ungár, G. Ribárik, L. Balogh, R. Thomas, O. Koc, M. Preuss, C.P. Race, P. Frankel, Fractional densities and character of dislocations in different slip modes from powder diffraction patterns, J. Nucl. Mater. 589 (2024) 154828, https://doi.org/10.1016/j.jnucmat.2023.154828.
[19] B.M. Jenkins, J. Haley, M.P. Moody, J.M. Hyde, C.R.M. Grovenor, APT and TEM study of behaviour of alloying elements in neutron-irradiated zirconium-based alloys, Scr. Mater. 208 (2022) 114323, https://doi.org/10.1016/j.scriptamat.2021.114323.
[20] A. Harte, M. Topping, P. Frankel, D. Jädernäs, J. Romero, L. Hallstadius, E. C. Darby, M. Preuss, Nano-scale chemical evolution in a proton-and neutron-irradiated Zr alloy, J. Nucl. Mater. 487 (2017) 30–42, https://doi.org/10.1016/j.jnucmat.2017.01.049.
[21] L. Tournadre, F. Onimus, J.L. Béchade, D. Gilbon, J.M. Cloué, J.P. Mardon, X. Feaugas, O. Toader, C. Bachelet, Experimental study of the nucleation and growth of c-component loops under charged particle irradiations of recrystallized Zircaloy-4, in: J. Nucl. Mater. (2012) 76–82, https://doi.org/10.1016/j.jnucmat.2011.11.061.
[22] H.L. Yang, S. Kano, J. McGrady, D.Y. Chen, K. Murakami, H. Abe, Microstructural evolution and hardening effect in low-dose self-ion irradiated Zr–Nb alloys, J. Nucl. Mater. 542 (2020) 152523, https://doi.org/10.1016/j.jnucmat.2020.152523.
[23] L.K. Mansur, Correlation of neutron and heavy-ion damage. II. The predicted temperature shift if swelling with changes in radiation dose rate, J. Nucl. Mater. 78 (1978) 156–160, https://doi.org/10.1016/0022-3115(78)90514-7.
[24] G.S. Was, J.T. Busby, T. Allen, E.A. Kenik, A. Jensson, S.M. Bruemmer, J. Gan, A. D. Edwards, P.M. Scott, P.L. Andreson, Emulation of neutron irradiation effects with protons: validation of principle, J. Nucl. Mater. 300 (2002) 198–216, https://doi.org/10.1016/S0022-3115(01)00751-6.
[25] O. El-Atwani, E. Esquivel, M. Efe, E. Aydogan, Y.Q. Wang, E. Martinez, S.A. Maloy, Loop and void damage during heavy ion irradiation on nanocrystalline and coarse grained tungsten: microstructure, effect of dpa rate, temperature, and grain size, Acta Mater 149 (2018) 206–219, https://doi.org/10.1016/j.actamat.2018.02.035.
[26] G.S. Was, Z. Jiao, E. Getto, K. Sun, A.M. Monterrosa, S.A. Maloy, O. Anderoglu, B. H. Sencer, M. Hackett, Emulation of reactor irradiation damage using ion beams, Scr. Mater. 88 (2014) 33–36, https://doi.org/10.1016/j.scriptamat.2014.06.003.
[27] P. Wang, J. Bowman, M. Bachhav, B. Kammenzind, R. Smith, J. Carter, A. Motta, E. Lacroix, G. Was, Emulation of neutron damage with proton irradiation and its effects on microstructure and microchemistry of Zircaloy-4, J. Nucl. Mater. 557 (2021) 153281, https://doi.org/10.1016/j.jnucmat.2021.153281.
[28] P. Saidi, M. Topping, C. Dai, F. Long, L.K. Béland, M.R. Daymond, The dependence of damage accumulation on irradiation dose rate in zirconium alloys: rate theory,

atomistic simulation and experimental validation, J. Nucl. Mater. 543 (2021) 152478, https://doi.org/10.1016/j.jnucmat.2020.152478.
[29] A. Jostsons, P.M. Kelly, R.G. Blake, The nature of dislocation loops in neutron irradiated zirconium, J. Nucl. Mater. 66 (1977) 236–256, https://doi.org/10.1016/0022-3115(77)90113-1.
[30] X. Yi, A.E. Sand, D.R. Mason, M.A. Kirk, S.G. Roberts, K. Nordlund, S.L. Dudarev, Direct observation of size scaling and elastic interaction between nano-scale defects in collision cascades, EPL 110 (2015), https://doi.org/10.1209/0295-5075/110/36001.
[31] D. Chen, K. Murakami, K. Dohi, K. Nishida, Z. Li, N. Sekimura, The effects of loop size on the unfaulting of Frank loops in heavy ion irradiation, J. Nucl. Mater. 529 (2020) 151942, https://doi.org/10.1016/j.jnucmat.2019.151942.
[32] T. Ungár, P. Frankel, G. Ribárik, C.P. Race, M. Preuss, Size-distribution of irradiation-induced dislocation-loops in materials used in the nuclear industry, J. Nucl. Mater. 550 (2021), https://doi.org/10.1016/j.jnucmat.2021.152945.
[33] M. Kirk, X. Yi, M. Jenkins, Characterization of irradiation defect structures and densities by transmission electron microscopy, J. Mater. Res. 30 (2015) 1195–1201, https://doi.org/10.1557/jmr.2015.19.
[34] T. Seymour, P. Frankel, L. Balogh, T. Ungár, S.P. Thompson, D. Jädernäs, J. Romero, L. Hallstadius, M.R. Daymond, G. Ribárik, M. Preuss, Evolution of dislocation structure in neutron irradiated Zircaloy-2 studied by synchrotron x-ray diffraction peak profile analysis, Acta Mater (2017), https://doi.org/10.1016/j.actamat.2016.12.031.
[35] M. Topping, T. Ungár, C.P. Race, A. Harte, A. Garner, F. Baxter, S. Dumbill, P. Frankel, M. Preuss, Investigating the thermal stability of irradiation-induced damage in a zirconium alloy with novel in situ techniques, Acta Mater (2017), https://doi.org/10.1016/j.actamat.2017.11.051.
[36] A.R. Warwick, R. Thomas, M. Boleininger, Ö. Koç, G. Zilahi, G. Ribárik, Z. Hegedues, U. Lienert, T. Ungar, C. Race, M. Preuss, P. Frankel, S.L. Dudarev, Dislocation density transients and saturation in irradiated zirconium, Int. J. Plast. 164 (2023) 103590, https://doi.org/10.1016/j.ijplas.2023.103590.
[37] Ö. Koc, R. Thomas, X. Liang, Z. Hegedues, U. Lienert, R.W. Harrison, M. Preuss, T. Ungar, P. Frankel, A spatially resolved analysis of dislocation loop and nanohardness evolution in proton irradiated zircaloys, Acta Mater. (2024), https://doi.org/10.2139/ssrn.4527582.
[38] R. Thomas, Ö. Koç, T. Ungár, G. Zilahi, Z. Hegedues, U. Lienert, G. Ribárik, H. Sharma, P. Kenesei, M. Preuss, P. Frankel, Characterization of irradiation damage using X-ray diffraction line-profile analysis, in: Zircon. Nucl. Ind. 20th Int. Symp., 2023, pp. 540–567, https://doi.org/10.1520/stp164520220056.
[39] R.E. Stoller, M.B. Toloczko, G.S. Was, A.G. Certain, S. Dwaraknath, F.A. Garner, On the use of SRIM for computing radiation damage exposure, Nucl. Instruments Methods Phys. Res. Sect. B Beam Interact. with Mater. Atoms. 310 (2013) 75–80, https://doi.org/10.1016/j.nimb.2013.05.008.
[40] E. Weckert, K. Balewski, W. Brefeld, W. Decking, W. Drube, H. Franz, P. Gürtler, U. Hahn, J. Pflüger, H. Schulte-Schrepping, M. Tischer, J. Schneider, PETRA III: a new high brilliance synchrotron radiation source at DESY, in: AIP Conf. Proc., 2004, pp. 73–76, https://doi.org/10.1063/1.1757737.
[41] G. Ashiotis, A. Deschildre, Z. Nawaz, J.P. Wright, D. Karkoulis, F.E. Picca, J. Kieffer, The fast azimuthal integration Python library: pyFAI, J. Appl. Crystallogr. 48 (2015) 510–519, https://doi.org/10.1107/S1600576715004306.
[42] T. Ungár, A. Borbély, The effect of dislocation contrast on x-ray line broadening: a new approach to line profile analysis, Appl. Phys. Lett. 69 (1996) 3173–3175, https://doi.org/10.1063/1.117951.
[43] T. Ungár, The meaning of size obtained from broadened x-ray diffraction peaks, Adv. Eng. Mater. 5 (2003) 323–329, https://doi.org/10.1002/adem.200310086.
[44] L. Balogh, G. Tichy, T. Ungár, Twinning on pyramidal planes in hexagonal close packed crystals determined along with other defects by X-ray line profile analysis, J. Appl. Crystallogr. 42 (2009) 580–591, https://doi.org/10.1107/S0021889809022936.
[45] G. Ribárik, B. Jóni, T. Ungár, The convolutional multiple whole profile (CMWP) fitting method, a global optimization procedure for microstructure determination, Crystals 10 (2020) 623, https://doi.org/10.3390/cryst10070623.
[46] M. Wilkens, The determination of density and distribution of dislocations in deformed single crystals from broadened X-ray diffraction profiles, Phys. Status Solidi. 2 (1970) 359–370, https://doi.org/10.1002/pssa.19700020224.
[47] P. Scardi, M. Leoni, Whole powder pattern modelling, Acta Crystallogr. Sect. A Found. Crystallogr. 58 (2002) 190–200, https://doi.org/10.1107/S0108767301021298.
[48] T. Ungár, L. Balogh, G. Ribárik, Defect-related physical-profile-based X-ray and neutron line profile analysis, in: Metall. Mater. Trans. A Phys. Metall. Mater. Sci. (2010) 1202–1209, https://doi.org/10.1007/s11661-009-9961-7.
[49] L. Balogh, D.W. Brown, P. Mosbrucker, F. Long, M.R. Daymond, Dislocation structure evolution induced by irradiation and plastic deformation in the Zr-2.5Nb nuclear structural material determined by neutron diffraction line profile analysis, Acta Mater 60 (2012) 5567–5577, https://doi.org/10.1016/j.actamat.2012.06.062.
[50] L. Balogh, F. Long, M.R. Daymond, Contrast factors of irradiation-induced dislocation loops in hexagonal materials, J. Appl. Crystallogr. 49 (2016) 2184–2200, https://doi.org/10.1107/S1600576716018136.
[51] G. Ribárik, T. Ungár, Characterization of the microstructure in random and textured polycrystals and single crystals by diffraction line profile analysis, Mater. Sci. Eng. A. 528 (2010) 112–121, https://doi.org/10.1016/j.msea.2010.08.059.
[52] I.C. Dragomir, T. Ungár, Contrast factors of dislocations in the hexagonal crystal system, J. Appl. Crystallogr. 35 (2002) 556–564, https://doi.org/10.1107/s0021889802009536.
[53] S.M. Hanlon, S.Y. Persaud, F. Long, A. Korinek, M.R. Daymond, A solution to FIB induced artefact hydrides in Zr alloys, J. Nucl. Mater. 515 (2019) 122–134, https://doi.org/10.1016/j.jnucmat.2018.12.020.
[54] M.K. Miller, K.F. Russell, G.B. Thompson, Strategies for fabricating atom probe specimens with a dual beam FIB, Ultramicroscopy 102 (2005) 287–298, https://doi.org/10.1016/j.ultramic.2004.10.011.
[55] K. Thompson, D. Lawrence, D.J. Larson, J.D. Olson, T.F. Kelly, B. Gorman, In situ site-specific specimen preparation for atom probe tomography, Ultramicroscopy 107 (2007) 131–139, https://doi.org/10.1016/j.ultramic.2006.06.008.
[56] A.J. London, Atom Probe Lab (2019). https://sourceforge.net/projects/atomprobelab/.
[57] O. Hellman, J. Vandenbroucke, J. Blatz Du Rivage, D.N. Seidman, Application software for data analysis for three-dimensional atom probe microscopy, Mater. Sci. Eng. A. 327 (2002) 29–33, https://doi.org/10.1016/S0921-5093(01)01887-1.
[58] B.M. Jenkins, J.O. Douglas, N. Almirall, N. Riddle, P.A.J. Bagot, J.M. Hyde, G. R. Odette, M.P. Moody, The effect of composition variations on the response of steels subjected to high fluence neutron irradiation, Materialia 11 (2020) 100717, https://doi.org/10.1016/j.mtla.2020.100717.
[59] T. Ungar, G. Ribarik, M. Topping, R.M.A. Jones, X.D. Xu, R. Hulse, A. Harte, G. Tichy, C.P. Race, P. Frankel, M. Preuss, Characterizing dislocation loops in irradiated polycrystalline Zr alloys by X-ray line profile analysis of powder diffraction patterns with satellites, J. Appl. Crystallogr. 54 (2021) 803–821, https://doi.org/10.1107/S1600576721002673.
[60] G. Ribárik, B. Jóni, T. Ungár, The convolutional multiple whole profile (CMWP) fitting method, a global optimization procedure for microstructure determination, Crystals 10 (2020) 623, https://doi.org/10.3390/cryst10070623.
[61] Y. Matsukawa, H.L. Yang, K. Saito, Y. Murakami, T. Maruyama, T. Iwai, K. Murakami, Y. Shinohara, T. Kido, T. Toyama, Z. Zhao, Y.F. Li, S. Kano, Y. Satoh, Y. Nagai, H. Abe, The effect of crystallographic mismatch on the obstacle strength of second phase precipitate particles in dispersion strengthening: bcc Nb particles and nanometric Nb clusters embedded in hcp Zr, Acta Mater 102 (2016) 323–332, https://doi.org/10.1016/j.actamat.2015.09.038.
[62] O.T. Woo, M. Griffiths, The role of Fe on the solubility of Nb in α-Zr, J. Nucl. Mater. (2009), https://doi.org/10.1016/j.jnucmat.2008.10.004.
[63] Z. Yu, A. Couet, M. Bachhav, Irradiation-induced Nb redistribution of ZrNb alloy: an APT study, J. Nucl. Mater. (2019), https://doi.org/10.1016/j.jnucmat.2019.01.015.
[64] S.B. Adisa, J. Hu, M.J. Swenson, APT characterization and modeling of irradiation-induced Nb-rich nanoclustering in Zr-1.0%Nb alloys, Materialia 16 (2021) 101040, https://doi.org/10.1016/j.mtla.2021.101040.
[65] M. Topping, A. Harte, T. Ungár, C.P. Race, S. Dumbill, P. Frankel, M. Preuss, The effect of irradiation temperature on damage structures in proton-irradiated zirconium alloys, J. Nucl. Mater. (2019), https://doi.org/10.1016/j.jnucmat.2018.12.006.
[66] S. Doriot, B. Verhaeghe, J.L. Béchade, D. Menut, D. Gilbon, J.P. Mardon, J. M. Cloué, A. Miquet, L. Legras, Microstructural evolution of M5™7 alloy irradiated in PWRs up to high fluences - comparison with other Zr-based alloys, ASTM Spec. Tech. Publ. STP 1543 (2015) 759–799, https://doi.org/10.1520/STP154320120179.
[67] V.O. Kharchenko, T. Xin, L. Wu, D.O. Kharchenko, V.V. Kupriienko, I.O. Shuda, Phase stability and precipitation modeling in neutron irradiated Zr-2% Nb alloy, Model. Simul. Mater. Sci. Eng. 30 (2022), https://doi.org/10.1088/1361-651X/ac8fad.
[68] E.R. Reese, N. Almirall, T. Yamamoto, S. Tumey, G. Robert Odette, E.A. Marquis, Dose rate dependence of Cr precipitation in an ion-irradiated Fe-18Cr alloy, Scr. Mater. 146 (2018) 213–217, https://doi.org/10.1016/j.scriptamat.2017.11.040.
[69] F. Soisson, E. Meslin, O. Tissot, Atomistic modeling of α' precipitation in Fe-Cr alloys under charged particles and neutron irradiations: effects of ballistic mixing and sink densities, J. Nucl. Mater. 508 (2018) 583–594, https://doi.org/10.1016/j.jnucmat.2018.06.015.
[70] R.W. Harrison, A.W. Carruthers, J.A. Hinks, M.G. Burke, S.E. Donnelly, Cascade size and dose rate effects on α′ precipitation in ion-irradiated Fe14Cr alloy, Scr. Mater. 172 (2019) 33–37, https://doi.org/10.1016/j.scriptamat.2019.06.034.
[71] Z. Yu, M. Bachhav, F. Teng, L. He, A. Couet, Nanoscale redistribution of alloying elements in high-burnup AXIOM-2 (X2®) and their effects on in-reactor corrosion, Corros. Sci. 190 (2021), https://doi.org/10.1016/j.corsci.2021.109652.
[72] J. Bowman, P. Wang, G.S. Was, M. Bachhav, A.T. Motta, Ion irradiation induced amorphization of precipitates in Zircaloy, J. Nucl. Mater. 571 (2022) 153988, https://doi.org/10.1016/j.jnucmat.2022.153988.
[73] G.P. Kobylyansky, A.E. Novoselov, A.V. Obukhov, Z.E. Ostrovsky, V.N. Shishov, M. M. Peregud, V.A. Markelov, Radiation damage of E635 alloy under high dose irradiation in the VVER-1000 and BOR-60 reactors, ASTM Spec. Tech. Publ. 1529 STP (2011) 827–849, https://doi.org/10.1520/stp49285t.
[74] R.M.A. Jones, The Effect of Niobium On the Microstructural Evolution of Zirconium Alloys During Proton Irradiation, The University of Manchester, 2019. https://www.research.manchester.ac.uk/portal/files/173358596/FULL_TEXT.PDF.
[75] Z. Yu, M. Bachhav, F. Teng, L. He, M. Dubey, A. Couet, STEM/EDS and APT study on the microstructure and microchemistry of neutron irradiated ZIRLOTM, J. Nucl. Mater. 573 (2023) 154139, https://doi.org/10.1016/j.jnucmat.2022.154139.
[76] D. Lee, E.F. Koch, Irradiation damage in Zircaloy-2 produced by high-dose ion bombardment, J. Nucl. Mater. 50 (1974) 162–174, https://doi.org/10.1016/0022-3115(74)90153-6.
[77] W. Jäger, H. Trinkaus, Defect ordering in metals under irradiation, J. Nucl. Mater. 205 (1993) 394–410, https://doi.org/10.1016/0022-3115(93)90104-7.

[78] J. Gao, K. Yabuuchi, A. Kimura, Characterization of ordered dislocation loop raft in Fe3+ irradiated pure iron at 300 °C, J. Nucl. Mater. 511 (2018) 304–311, https://doi.org/10.1016/j.jnucmat.2018.09.020.
[79] G.L. Kulcinski, J.L. Brimhall, Ordered defect structures in irradiated metals, ASTM Spec. Tech. Publ (1972) 258–271, https://doi.org/10.1520/stp35452s.
[80] C. Dai, P. Saidi, M. Topping, L.K. Béland, Z. Yao, M.R. Daymond, A mechanism for basal vacancy loop formation in zirconium, Scr. Mater. 172 (2019) 72–76, https://doi.org/10.1016/j.scriptamat.2019.07.006.
[81] V.N. Shishov, The evolution of microstructure and deformation stability in Zr-Nb-(Sn,Fe). alloys under neutron irradiation, J. ASTM Int. 7 (2010) 37–66, https://doi.org/10.1520/JAI103005.
[82] B.A. Gurovich, A.S. Frolov, E.A. Kuleshova, D.A. Maltsev, D.V. Safonov, E. V. Alekseeva, TEM-studies of the dislocation loops and niobium-based precipitates in E110 alloy after operation in VVER-type reactor conditions, Mater. Charact. 150 (2019) 22–30, https://doi.org/10.1016/j.matchar.2019.01.014.
[83] M. Griffiths, J.F. Mecke, J.E. Winegar, Evolution of microstructure in zirconium alloys during irradiation, ASTM Spec. Tech. Publ. 1295 (1996) 580–602, https://doi.org/10.1520/stp16191s.
[84] A.V. Barashev, S.I. Golubov, R.E. Stoller, Theoretical investigation of microstructure evolution and deformation of zirconium under neutron irradiation, J. Nucl. Mater. 461 (2015) 85–94, https://doi.org/10.1016/j.jnucmat.2015.02.001.
[85] V.N. Shishov, M.M. Peregud, A.V. Nikulina, V.F. Kon'Kov, V.V. Novikov, V. A. Markelov, T.N. Khokhunova, G.P. Kobylyansky, A.E. Novoselov, Z.E. Ostrovsky, A.V. Obukhov, Structure-phase state, corrosion and irradiation properties of Zr-Nb-Fe-Sn system alloys, J. ASTM Int. 5 (2008) 724–743, https://doi.org/10.1520/JAI101127.